Measurement of Deformation in Geosynthetic Reinforced Loose Sand under Hydraulic Loading using Physical and Numerical modeling

Forough Ashkan

Department of Civil Engineering, University of Maragheh, Maragheh, Iran.

Received: **30.04.2025** Accepted: **20.05.2025** Published: **11.06.2025**

Turkish Journal of Hydraulics, Issue: **9 No**:**1** pp. **01–15** (2025)

e-ISSN: 2636-8382

SLOI: http://www.dergipark.gov.tr

ashkan@maragheh.ac.ir

Abstract

Reinforced soil structures have proven to be an effective solution in various hydraulic applications such as coastal retaining walls, earth dams, canal linings, settling basins, and irrigation and drainage networks. This study investigates the enhancement of bearing capacity in foundation systems situated on sandy subsoil reinforced with geosynthetics. A series of experimental models were developed to examine the performance of strip footings on both reinforced and unreinforced sand, focusing on key variables such as reinforcement type (geogrid vs. geotextile), number of reinforcement layers, depth of the first layer, and spacing between layers. To validate and extend the physical results, numerical simulations were performed using Plaxis v8.2. The results indicate that geogrid reinforcement provides superior bearing performance compared to geotextile and unreinforced conditions, particularly in hydraulic structures subject to fluctuating loads and moisture conditions. The PIV method was applied to monitor soil displacement patterns, and the numerical findings showed good agreement with physical observations. The increased volume of the failure zone due to reinforcement was found to contribute significantly to bearing capacity improvement, which is crucial for ensuring the long-term stability of hydraulic infrastructures.

Keywords: Strip foundation, Reinforced sand, Hydraulic loading, Experimental modeling (PIV), Plaxis software.

1. INTRODUCTION

Soil is a natural material that exhibits high resistance to compressive and shear forces but has relatively low resistance to tensile stresses. To overcome this inherent weakness, various soil reinforcement methods have been developed. Reinforced soil is composed of two distinct materials: soil and a reinforcing medium. In this study, geogrids are a type of geosynthetic material that is used as reinforcement. These reinforcements enhance the tensile strength of the soil, thereby reducing shear deformations and improving the overall stability of the soil mass.

However, in certain applications, such as irrigation networks or flood-prone areas, the soil may become saturated. Therefore, the drainage characteristics of the reinforcement materials must be carefully considered when designing reinforced soil systems. If the native soil lacks sufficient drainage capacity, reinforcement materials should be selected to compensate for this deficiency [1].

Numerous studies have investigated the behavior of reinforced soil under various loading conditions. One of the earliest significant contributions in this field was made by Huang and Menq, who developed an analytical method based on limit equilibrium theory to study the behavior of reinforced soils under tensile forces. Their analysis examined the effects of reinforcement parameters and soil properties on the mechanical response of reinforced systems, and their proposed model showed good agreement with experimental laboratory results [2,3].

Similarly, Yamamoto studied the gradual failure behavior of reinforced foundations. Using laboratory-scale physical models constructed with aluminum samples, he investigated the influence of the length and material characteristics of reinforcements on foundation performance. His findings indicated that both the ultimate bearing capacity and the evolution of the failure zone are significantly influenced by factors such as the stiffness, number of reinforcement layers, and depth of placement of the reinforcing materials [4].

Moghaddas-Tafreshi and Dawson investigated the bearing capacity of strip foundations on sand reinforced with geosynthetics, specifically geogrids and geotextiles.

They analyzed various reinforcement parameters, including the number of reinforcement layers, the vertical spacing between layers, and the depth of the first reinforcement layer [5].

In addition to bearing capacity, they also evaluated the settlement behavior of the reinforced foundations. Their results showed that increasing the number of reinforcement layers, placing the first reinforcement layer deeper, and using geogrid materials significantly enhanced the bearing capacity and reduced settlement. Overall, their findings demonstrated that geogrid reinforcements performed better than geotextiles, offering higher strength and more effective settlement control. Therefore, geogrids were recommended for improving the bearing capacity and reducing settlement in strip foundations compared to geotextiles.

Qiming and Murad proposed an analytical approach to estimate the ultimate bearing capacity of reinforced strip foundations. Their study introduced a general failure mechanism for reinforced foundations, based on an equilibrium analysis of the foundation-reinforcement system and the progressive development of shear failure zones. The study revealed that the depth of the critical shear failure surface (denoted as DP) is closely related to the relative shear strength of the reinforced and unreinforced soil layers and is consistently influenced by the reinforcement ratio (Rr) [6,7].

In addition, Hajialilue-Bonab et al. investigated the failure mechanism, shear strain distribution, and the effects of reinforcement on the behavior of reinforced sand beneath strip foundations using the Particle Image Velocimetry (PIV) method. In their study, a physical model was prepared with dry sand, and geosynthetic materials were used for soil reinforcement. Their findings provided valuable insights into the deformation behavior and reinforcement efficiency in strip foundations [8].

In every loading case, the behavior of the foundation soil was analyzed using digital modeling and failure images were captured. The results of the studies indicate that the use of appropriate reinforcements significantly improves the bearing capacity, reduces settlement, and improves the overall stiffness of the soil. Additionally, the performance of geogrids was found to be superior to geotextiles in sandy soils and in small-scale foundation models.

The results, as reported in various studies, show that increasing the number of reinforcements and adjusting their placement in the foundation area leads to an improvement in the soil's bearing capacity. Furthermore, the study demonstrated the effects of different reinforcements on the behavior of the soil and their influence on the settlement and stability of the foundation under loading.

For evaluation of the effects, PIV (Particle Image Velocimetry) was used to measure the soil deformation in the physical model, and further analysis was conducted with the PLAXIS software, as well as using numerical simulations. The results confirmed that the placement of reinforcements leads to a noticeable improvement in the stability and performance of the reinforced foundation, and the comparison of two models indicates that the improved stiffness of the soil with reinforcement matches the expected results for both cases.

In recent years, numerous studies have investigated the behavior of reinforced soils under various loading conditions. One of the prominent studies in this field was conducted by Ranjan et al., which focused on the stability and deformation analysis of composite retaining walls consisting of mechanically stabilized earth (MSE) walls and soil-nailed (SN) walls [9].

In this study, the finite element method and reliability-based analysis were used to examine the impact of design parameters on the performance of the composite wall. The results indicated that the wall height and reinforcement length in both MSE and SN walls significantly influence the stability of the composite system. Moreover, the soil friction angle and the coefficient of variation of critical parameters had a notable effect on the wall's reliability. To assist designers in achieving the desired level of reliability, reliability-based design charts were developed, which present the ratio of the MSE wall reinforcement length to the total wall height for critical parameters.

Another study by Lin et al. investigated the strain characteristics of reinforced soft clay surrounding tunnels under metro loads. This research utilized dynamic soil testing to analyze the strain behavior of reinforced soft clay. The findings showed that metro loads significantly affect soil strain characteristics, and the use of reinforcements can enhance the dynamic performance of the soil [10]. Additionally, Li et al. examined the structural behavior of reinforced retaining walls under combined effects of rainfall and earthquakes. In this study, shake table tests were conducted to analyze the performance of modular panel reinforced retaining walls under different rainfall and seismic conditions. The results demonstrated that rainfall can considerably influence the seismic performance of retaining walls, and under saturated conditions, the seismic stability of the wall decreases. These findings can aid in the multi-hazard risk assessment of modular panel reinforced retaining walls [10].
Khawaja et al. found that accurate prediction of the modulus of resilience (MR) of subgrade soils exhibiting nonlinear stress-strain behaviors is crucial for effective soil assessment. Traditional laboratory techniques for determining MR are often costly and time-consuming. They investigated the effectiveness of genetic programming (GEP), polynomial programming (MEP), and artificial neural networks (ANN) in predicting MR using 2813 data records, considering six key parameters. The results showed that the GEP model consistently outperformed the MEP and ANN models, showing the lowest error measures and the highest correlation indices (R2) [11].

These studies demonstrate that the behavior of reinforced soils under different loading conditions—including dynamic loads, metro loads, and combined effects of rainfall and earthquakes is complex and requires detailed analysis using advanced methods such as finite element modeling and reliability-based analysis. The use of reinforcements, such as geogrids and soil nails, can contribute to improved stability and dynamic performance of soils.

These findings are particularly important for the design and analysis of reinforced soil structures, especially in regions prone to natural hazards such as earthquakes and heavy rainfall.

2. METHODOLOGY

2.1. Specifications of the Laboratory Model

In this study, dry sand collected from the Sufian region in East Azerbaijan, located in the northwest of Iran, was utilized. To ensure proper saturation and obtain reliable results from the physical model tests, the samples were prepared with a relative density ranging from 15 to 50 percent.

For the determination of the soil characteristics, grain size analysis was conducted according to ASTM D 422-87. The results indicate that the soil has a $\emptyset = 26.82$ Degree and c =0.33 (kpa) and with a unit specific weight (Gs = 2.67) with a unit weight in the loose condition 1.5 g/cm³. The tested sand, having a uniformity coefficient (Cu=1.25) and a coefficient of gradation (Cc=0.996), was classified as a poorly graded sand (SP) according to the Unified Soil Classification System (USCS). The grain size curve of this soil is shown (Figure 1).

For the estimation of the modulus of elasticity (E) of the soil, an approach based on artificial neural network (ANN) proposed by was used, which is considered a quick, cost-effective, and reliable model for evaluating this property. The model inputs include soil index properties such as particle size distribution, plastic limit, liquid limit, unit weight, and specific gravity . The ANN model's performance was compared with that of multiple regression models, and it was found to outperform them.

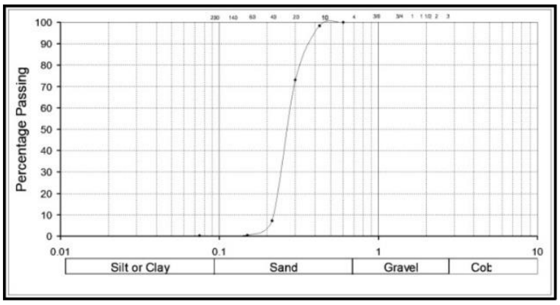

Figure 1. Grain size distribution curve of sand soil

In the reinforced soil foundation model tests, two types of reinforcements were used: geogrids and geotextiles. Given the specific wave conditions in the model setup, a reinforced concrete strip foundation was first created with a length of 1.8 meters, a width of 0.40 meters, and a height of 0.50 meters has been created.

Reinforcements with 6 bolts were placed at both ends of the foundation, which were later incorporated into the test setup to ensure the foundation's proper alignment for subsequent laboratory testing.

Similarly, the arrangement of the connections and the joints were designed. As shown in the figure, for the connection of two 160 UNP beams and for the connection of two 200 UNP beams, a specific arrangement was applied. Afterward, the beams and connections were reinforced using straps and bolts.

Figure 2 shows the support system used for the arrangement.

For the laboratory testing setup, which required the soil to be placed inside, a metal frame with a thickness of 3.9 cm was used. Given the thickness and connection method, it was designed to ensure proper structural stability. This frame was used in the dimensions 1 × 0.30 meters in the main testing area, and 0.60 × 0.30 meters along the sides, and 1 × 0.60 meters behind the setup. To prevent lateral wall displacement due to the soil's lateral pressure, additional plates were applied with dimensions of 5.13 cm in width and 3.34 cm in thickness, which were connected to the inner part of the walls

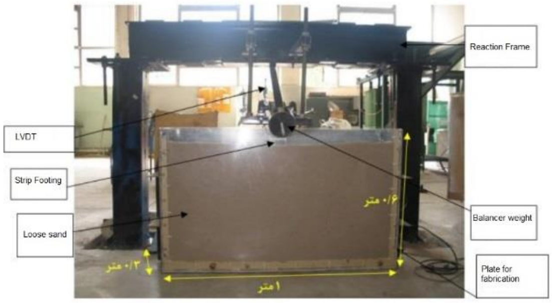

Figure 2. Jack Support Structure and Scaled Physical Model Chamber.

. For the testing system in the loading process, a system with dimensions of 60 × 100 cm and a thickness of 3 cm was applied, ensuring that the setup remained visibly stable. A loading system with control was used to apply pressure, and the respective deformation was monitored through sensors. The load system had a capacity of 1.03 × 1.0 meters with a thickness of 0.03 meters, and weights of 3 kilograms were added to balance the system.

The applied load affects the center of the rigid foundation, and a digital load cell was used to precisely measure the force. For monitoring the applied pressure to the soil, a metal sheet of 3.06 cm thickness and 0.30 × 0.61 meters in size was used as the foundation under the test setup, functioning as the base layer over the soil.

To measure the settlement, a digital displacement sensor (LVDT) was used, which was placed on the plate and close to its center. The readings from the sensor were used to determine the settlement of the plate.

Figure 3 shows the number of reinforcement layers (N), the depth of the reinforcement layer (u), and the width of the reinforcement layers (b) and Strip footing width (B) for the rigid foundation. The schematic of the experimental model is shown in Figure 3.

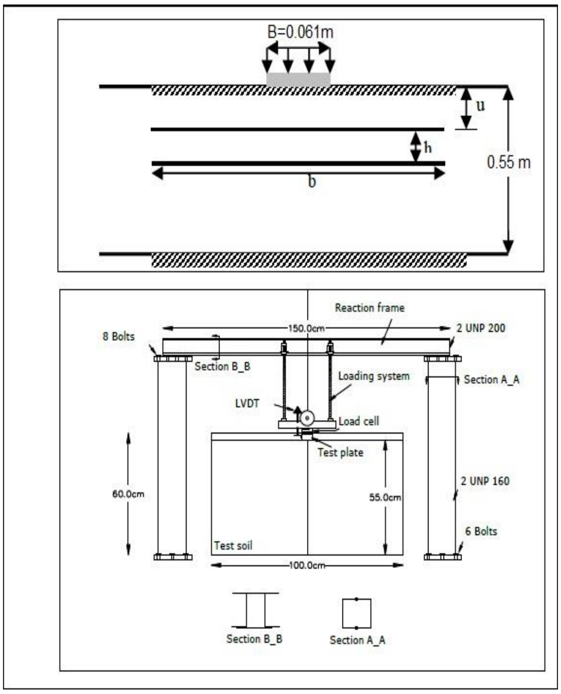

Figure 3a and 3b. Parameters and Schematic of the Experimental Model

To ensure uniformity in the model and the appropriate consistency in the soil's compaction, it was required that the soil compaction be linear and uniform in all models.

The method used followed a sequential process of compaction and arrangement, ensuring uniformity throughout. After the soil was compacted, each reinforcement was placed in its designated position.

Following this, the soil compaction continued until reaching the desired level. The rigid foundation was carefully placed on the soil surface, and the loading system was installed. Once the load application system was set, the system was ready for the test.

For each load application, measurements were taken to ensure that both the load and the settlement stabilized, and once they did, data was recorded using a digital data logger and processed through the Geopiv8 software [11]. In this study, the obtained displacement data were used to generate 48×48 image grids, which were then used to analyze the displacement in the soil mass, as shown in the schematic in Figure 3.

2.2. Soil Deformation and Strength Analysis

The soil deformation and its associated strength characteristics were analyzed, focusing on the influence of reinforcement parameters, such as the type of geogrid or geotextile, number of layers, and the effect of varying conditions. The parameters for the experimental model and numerical values are presented in Table 1, and the reinforcement specifications used are outlined in Table 2 (Table 2). In Table 1, geotextiles are represented by parameter A and geogrids by parameter B (Table 1).

Table 1. Summary of Experimental Conditions for Reinforced and Unreinforced Strip Footings

Test No.	Type of Reinforcement	N	b/B	u/B	h/B
1	Geotextile	1	15	0.5	-
2	Geotextile	1	15	0.25	-
3	Geotextile	2	15	0.5	0.5
4	Geotextile	1	15	1	-
5	Geotextile	1	11	0.5	-
6	Geotextile	1	9	0.5	-
7	Geogrid	1	15	0.5	-
8	Unreinforced	-	-	-	-
9	Geotextile	2	11	0.5	0.5
10	Geogrid	1	11	0.5	-

2.3. Numerical Simulation

For the numerical analysis, the finite element method was used, employing the PLAXIS v8.2 software. Given its compatibility and soil behavior modeling features, this software was chosen for the simulation. For the soil model, the Mohr-Coulomb model was used under undrained conditions, and for greater accuracy, 15-node elements were employed in the model. Geogrid reinforcements were modeled as geogrid elements, considering their capacity to carry tensile forces.

Two primary conditions were modeled: a wall and a foundation with reinforcement. Appropriate boundary conditions were applied to ensure realistic modeling of soil behavior under loading conditions.

Table 2. Properties of Sandy Soil, Reinforcement Material, and Foundation Used in Experimental and Numerical Models.

Parameter	Unit	Value
Internal friction angle of sandy soil $\emptyset$	(°)	26.82
Unit weight of sand	(kN/m³)	15
Interface friction coefficient between soil and reinforcement	(–)	0.9
Particle density G_s	-	2.67
Weight of reinforcement	(g/m²)	300
Thickness of reinforcement	(mm)	1.6
Ultimate tensile strength of geotextile and geogrid	(kN/m)	55, 13
Elastic modulus of sandy soil (E)	(kPa)	8000
Axial stiffness of geotextile and geogrid (EA)	(kN/m)	1500,1000

2.4. Soil-Structure Interaction and Model Behavior

To simulate the interaction between the soil and the structure, various boundary conditions and load applications were tested. This allowed for a comprehensive understanding of the reinforcement's effects, including the reduction of settlements in reinforced soil and the impact on the stability of the system. Additionally, to accurately simulate the soil's behavior, the influence of various reinforcements, such as geogrids and geotextiles, was carefully assessed and incorporated into the model.

The study provides a detailed analysis of the various parameters involved in soil reinforcement and its effects on settlement and soil strength, offering valuable insights for future geotechnical applications.

3. Results and Discussion

3.1. Effect of Reinforcement Type on Bearing Capacity of Strip Footing in Physical and Numerical Models

Figure 4 presents the settlement curves for strip footings in both unreinforced soil and soil reinforced with geotextiles and geogrids for the physical and numerical models. The graphs show the applied pressure (q) in kilopascals and the settlement (s) in millimeters.

In this study, two types of reinforcements geotextile and geogrid were utilized. For geotextile, the resistance to sliding between the soil and the geotextile at the contact interface is considered. In contrast, for geogrid, the resistance to sliding is generated both by the sliding of the soil over the geogrid and the interaction between the geogrid material itself and the soil.

Therefore, the shear resistance created in the soil-geogrid system is typically higher than the shear resistance in the geotextile system.

Figure 4 illustrates the settlement values under the applied pressure for the two types of reinforcements. It also shows the settlement at a depth of u = 30 mm for unreinforced soil, indicating the variation in settlement with and without reinforcement.

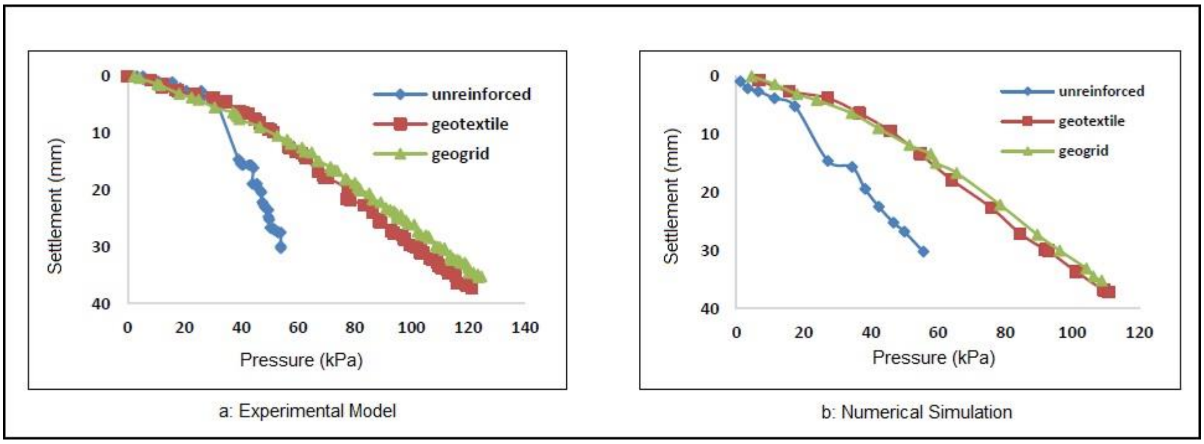

Figure 4a and b. Pressure-settlement diagrams for geotextile and geogrid reinforcements, and unreinforced soil in physical and numerical models

In Figure 4, the geogrid-reinforced curve is positioned below the geotextile curve at lower applied pressures of up to 50 kPa. For pressures above 50 kPa, geogrid reinforcement shows a superior performance compared to the geotextile reinforcement. According to Guido et al. [14], at lower pressures, reinforcements with lower tensile resistance perform better than those with higher tensile resistance.

The comparison of geotextile and geogrid reinforcement shows that the reinforced foundation performs better than the unreinforced soil. At a pressure of 36 kPa, the unreinforced foundation exhibits significant settlement with increasing pressure, while the reinforced foundations (geogrid and geotextile) show a more stable behavior.

In the case of the unreinforced foundation, settlement gradually increases with pressure. However, when the applied pressure reaches 36 kPa, sudden jumps in settlement are observed, indicating that failure or collapse is approaching. Meanwhile, for the geogrid-reinforced foundation, the settlement remains more controlled, and no sudden collapse occurs even up to 124 kPa. Similarly, for the geotextile reinforcement, failure does not occur until the applied pressure reaches around 121 kPa.

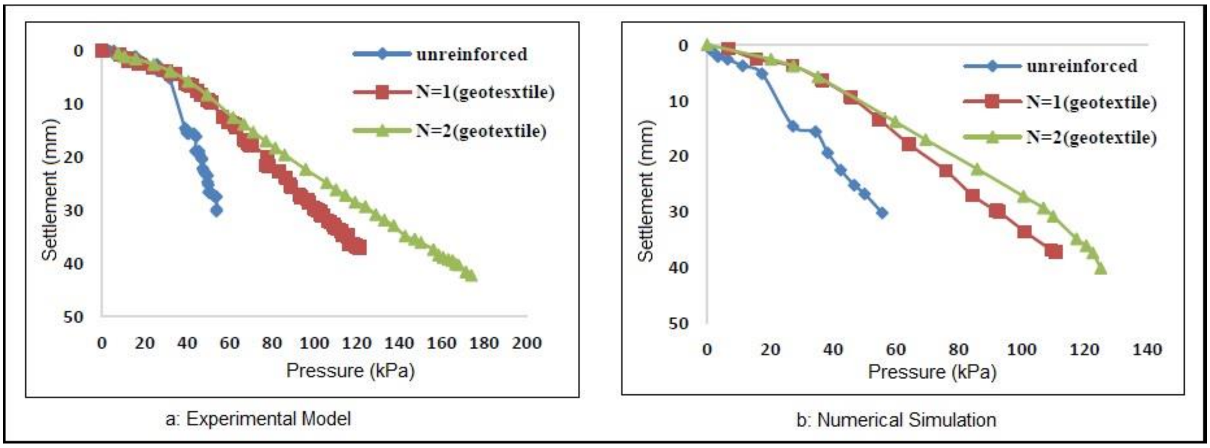

Figure 5. Effect of reinforcement layers on the bearing capacity of strip foundations in a) Experimental models and b) Numerical models

In Figure 5, the results show the influence of reinforcement layers on the settlement of strip foundations. For the physical model (Figure 5a), when two geotextile layers are used, the settlement at an applied pressure is lower compared to the case with a single geotextile layer. This indicates that increasing the number of reinforcement layers makes the foundation more stable and reduces the settlement under load. As the number of layers increases, the soil beneath the foundation becomes more compacted, which results in reduced displacement.

In the numerical model (Figure 5b), similar trends are observed. The curve for two layers of geotextile reinforcement shows less settlement than the curve for a single layer, indicating that more reinforcement helps distribute the load more evenly across the soil, reducing the settlement. This outcome suggests that adding layers of geotextile reinforcement enhances the performance of the foundation, making it more effective in preventing excessive settlement.

The comparison between the physical and numerical models confirms that both models demonstrate a consistent reduction in settlement with the addition of geotextile layers. The results highlight that increasing the number of reinforcement layers can significantly improve the bearing capacity and reduce the settlement of strip foundations under applied loads.

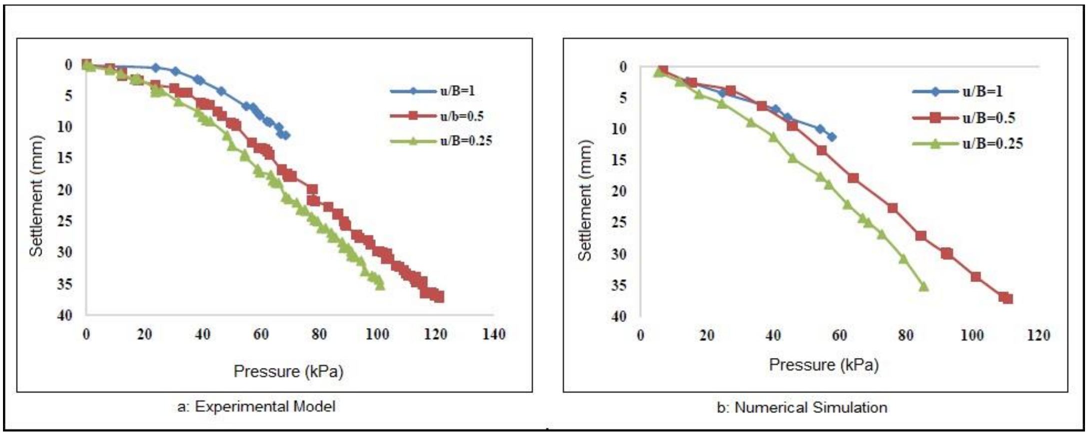

Figure 6. Effect of reinforcement depth on the bearing capacity of strip foundations in a) Experimental models and b) Numerical models

In Figure 6a, the relationship between the applied pressure and settlement for a strip foundation with one layer of geotextile reinforcement is shown in the physical model. The curve for $\frac{u}{B} = 1$ (where $\frac{u}{B}$ represents the depth ratio of the reinforcement) shows better performance in terms of reduced settlement up to a pressure of 70 kPa, compared to the other two curves. After this point, however, the curve with $\frac{u}{B} = 0.5$ shows a lower settlement under the same applied pressure, indicating that deeper reinforcement layers provide better overall performance in preventing settlement.

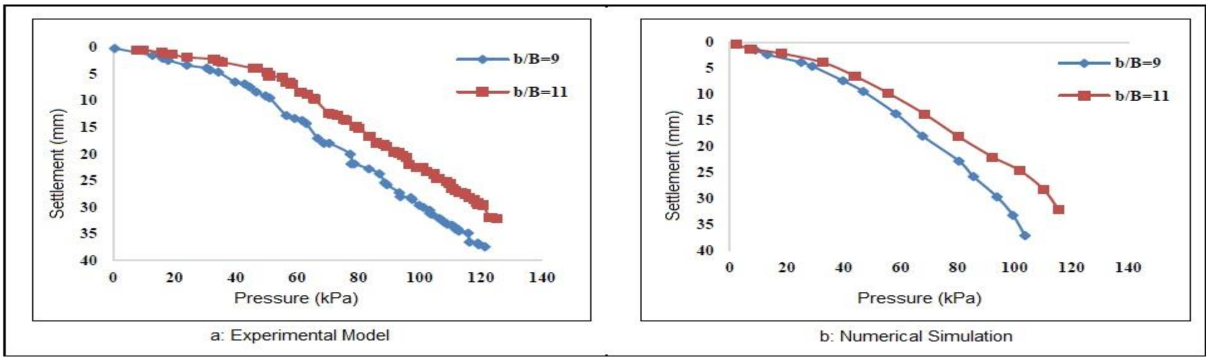

Figure 7. Effect of reinforcement width on the bearing capacity of strip foundations in a) Experimental models and b) Numerical models

Figure 6b presents the numerical model results, where a similar trend is observed. The curve for $\frac{u}{B} = 1$ shows better performance under lower applied pressures, while the curve for $\frac{u}{B} = 0.5$ outperforms the others at higher pressures. This suggests that for deeper layers of reinforcement, the settlement is better controlled across a broader range of applied pressures.

Both the physical and numerical models demonstrate that increasing the depth of the reinforcement layer improves the bearing capacity of the foundation, particularly at higher applied pressures. The results indicate that deeper reinforcement layers help distribute the load more effectively, thereby reducing settlement more effectively than shallow reinforcement layers.

Figure 7a illustrates the relationship between the applied pressure and settlement for different reinforcement widths (b/B=11,9) with one layer of geotextile reinforcement at a depth of 30 mm on a cohesive soil bed. It shows that as the reinforcement width (b/B) increases, the settlement at lower applied pressures does not exhibit a significant increase. However, as applied pressure increases, a lower settlement is observed for foundations with wider reinforcement widths, indicating improved performance with wider reinforcement.

Figure 7b presents the numerical model results, which follow a similar trend. It confirms that a wider reinforcement significantly enhances the bearing capacity of the foundation, resulting in less settlement under the same applied pressure. As the contact area between the soil and the reinforcement material increases, the shear resistance generated at the interface also increases, improving the overall performance of the soil and reinforcement system.

In both experimental and numerical models, increasing the width of the reinforcement leads to an increase in the bearing capacity of the soil, with reduced settlement under higher applied pressures. This indicates that reinforcement width plays a key role in enhancing the performance of strip foundations, especially under high loads.

In your analysis, the parameter UBCR (Ultimate Bearing Capacity Ratio) is used to compare the bearing capacities of reinforced and unreinforced strip foundations. This ratio is defined as:

UBCR=qr/qu

Where:

- qr is the ultimate bearing capacity in the reinforced condition (with geotextile or geogrid).
- qu is the ultimate bearing capacity in unreinforced conditions (without reinforcement).

For a given settlement (such as 30 mm), you're calculating how reinforcement affects the bearing capacity by comparing these two values. This allows you to quantify the improvement in the foundation's capacity due to the type of reinforcement and the number of layers used.

Based on your analysis in Figures 8 and 9:

- In Figure 8:

As shown in Figure 8a, by changing the type of reinforcement in u/B=0.5, the average value of the UCBR has approximately reached 2.01 for the geogrid and 1.83 for the geotextile.

Figure 8b shows the effect of the number of reinforcements on one and two layers of geotextiles. As seen in the figure, the UBCR is approximately 2.27 for two layers and 1.83 for one layer of geotextiles on average.

- In Figure 9:

In Figure 9a, it can be observed that by changing the type of reinforcement, the UBCR is approximately 1.79 for geogrid and 1.7 for geotextile on average.

Figure 9b illustrates the effect of the number of reinforcements for one and two layers of geotextile. As can be seen from the figure, the UBCR is approximately 2.09 for two layers and 1.71 for one layer of geotextile on average.

This data shows how both the type of reinforcement and the number of layers affect the bearing capacity of the foundation. Multiple layers, especially geotextile, significantly improve performance. Additionally, geogrid reinforcement tends to be more effective in enhancing bearing capacity than geotextile reinforcement.

In Figures 8 and 9, the variations in the Ultimate Bearing Capacity Ratio (UBCR) are observed for physical and numerical models, respectively, highlighting the influence of different reinforcement types and the number of layers:

- Figure 8 (Physical Model):

The UBCR for geogrid reinforcement increases with the number of reinforcement layers, showing significant improvements compared to a single geotextile layer.

- Figure 9 (Numerical Model):

Similar trends are observed in the numerical model, where multiple layers of geogrid reinforcement provide enhanced bearing capacity compared to single-layer reinforcements.

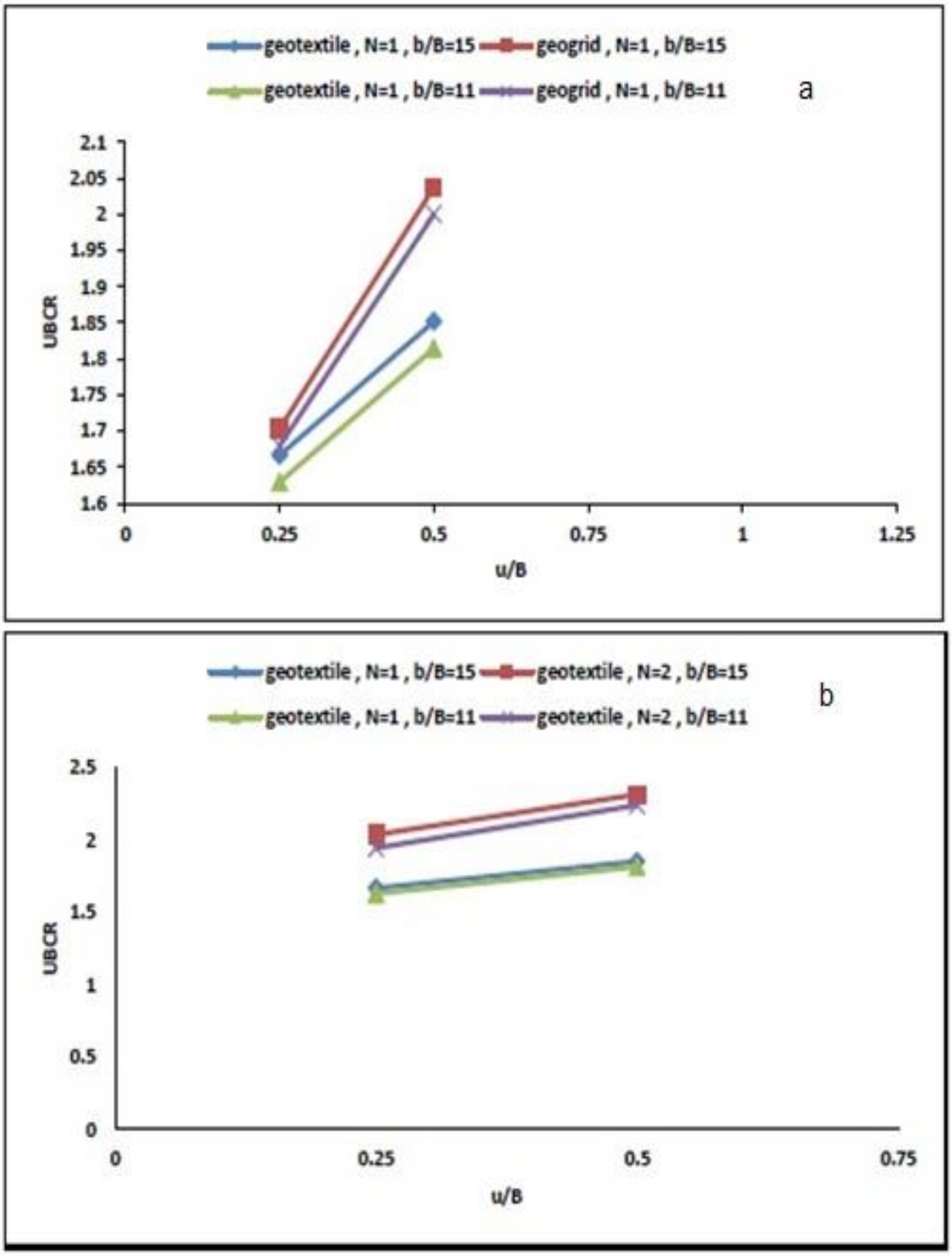

Figures 8. Graphs of the variation in the Ultimate Bearing Capacity Ratio (UBCR) of the strip footing in the experimental model (a: geogrid b: geotextile)

Regarding Figure 10 and the behavior of soil deformation:

- In Figure 10a (PIV Analysis of Displacements):

    The displacement vectors illustrate the extent and depth of soil deformation under various conditions.

    For reinforced conditions, displacement vectors extend more compared to unreinforced ones.

    The shear failure zone near the foundation edge in the unreinforced case shows more localized deformation compared to the reinforced case.

- In Figure 10b, under reinforced conditions (using a geotextile):

The displacement vectors follow the same trend, indicating the enhanced performance of reinforced soil over unreinforced soil, especially at greater depths.

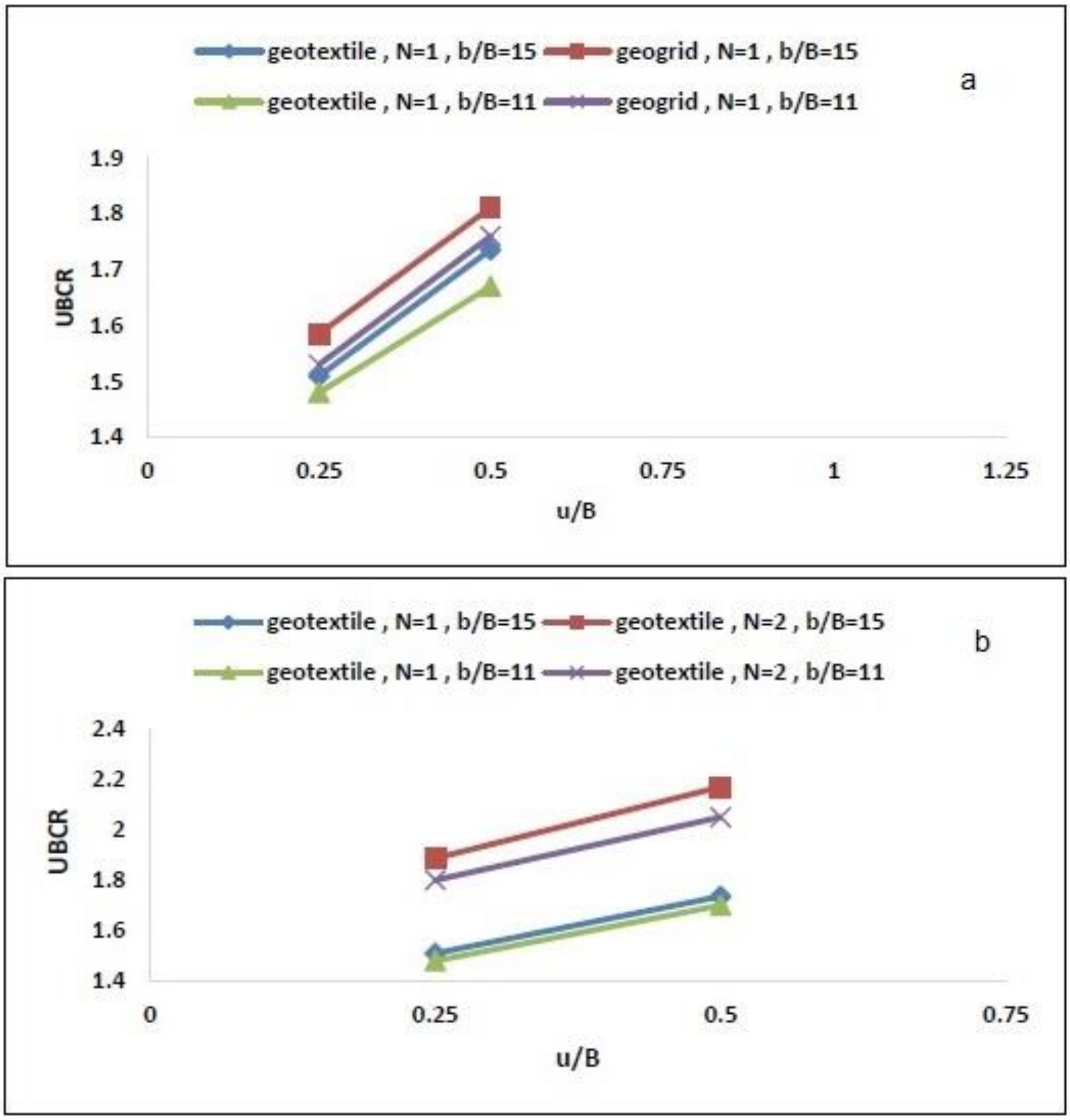

Figures 9. Graphs of the variation in the Ultimate Bearing Capacity Ratio (UBCR) of the strip footing in the numerical model (a: geogrid b: geotextile)

- Figures 10c and 10d (Plaxis Simulation):

The displacement vectors in Plaxis show reduced displacement at deeper layers with reinforcement. The direction of the displacement vectors is aligned with the load direction in the reinforced case.

These figures help to visualize the significant impact of reinforcement on soil behavior, showing better load distribution and less deformation in reinforced soils, both in physical and numerical models.

In the discussion section, the following observations are made regarding soil behavior under different reinforcement conditions:

- The displacement vectors in the reinforced soil show greater depth and more extended deformation zones compared to the unreinforced case. The failure zone shifts significantly with reinforcement, especially under the influence of geotextile reinforcement, indicating a more controlled deformation process.

- Shear failure in the unreinforced soil is observed to be more localized near the foundation, while for the reinforced soil, this failure zone spreads out more evenly. This demonstrates that reinforcement helps in distributing the load more effectively across the foundation area.

- Increased depth and width of deformation are noted in the reinforced cases (both geogrid and geotextile), with the reinforcement improving the soil's bearing capacity. As depth increases, the deformation becomes more contained and less pronounced in the reinforced soil.

- The reinforced layer, especially with geotextiles, leads to a more uniform and stable distribution of displacement vectors, which ultimately results in better performance and increased bearing capacity. The reinforcement effectively mitigates excessive settlement and provides a more controlled response to applied loads.

These findings suggest that reinforcement, particularly with geotextiles, helps improve the soil's ability to resist deformation underload and increases the foundation's bearing capacity. The depth and width of failure zones are significantly reduced in reinforced conditions, leading to a more stable and effective foundation system.

S represents a settlement of 30 millimeters.

Table 3. Effect of Reinforcement Type and Quantity on UBCR Changes in Experimental and Numerical Models at a Settlement Depth of 30 mm

Reinforcement Condition	Settlement Depth (mm)	UBCR (Experimental)	UBCR Change (%)	UBCR (Numerical)	UBCR Change (%)
No reinforcement	30	1.00	–	1.00	–
One layer of geotextile	30	1.23	+23.00	1.20	+20.00
One layer of geogrid	30	1.31	+31.00	1.27	+27.00
Two layers of geotextile	30	1.37	+37.00	1.35	+35.00
Two layers of geogrid	30	1.44	+44.00	1.40	+40.00

This table demonstrates the effect of the type and number of reinforcements on the changes in UBCR in both experimental and numerical models at a settlement depth of 30 millimeters.

The table summarizes the information regarding the depth of settlement and the variations under different conditions.

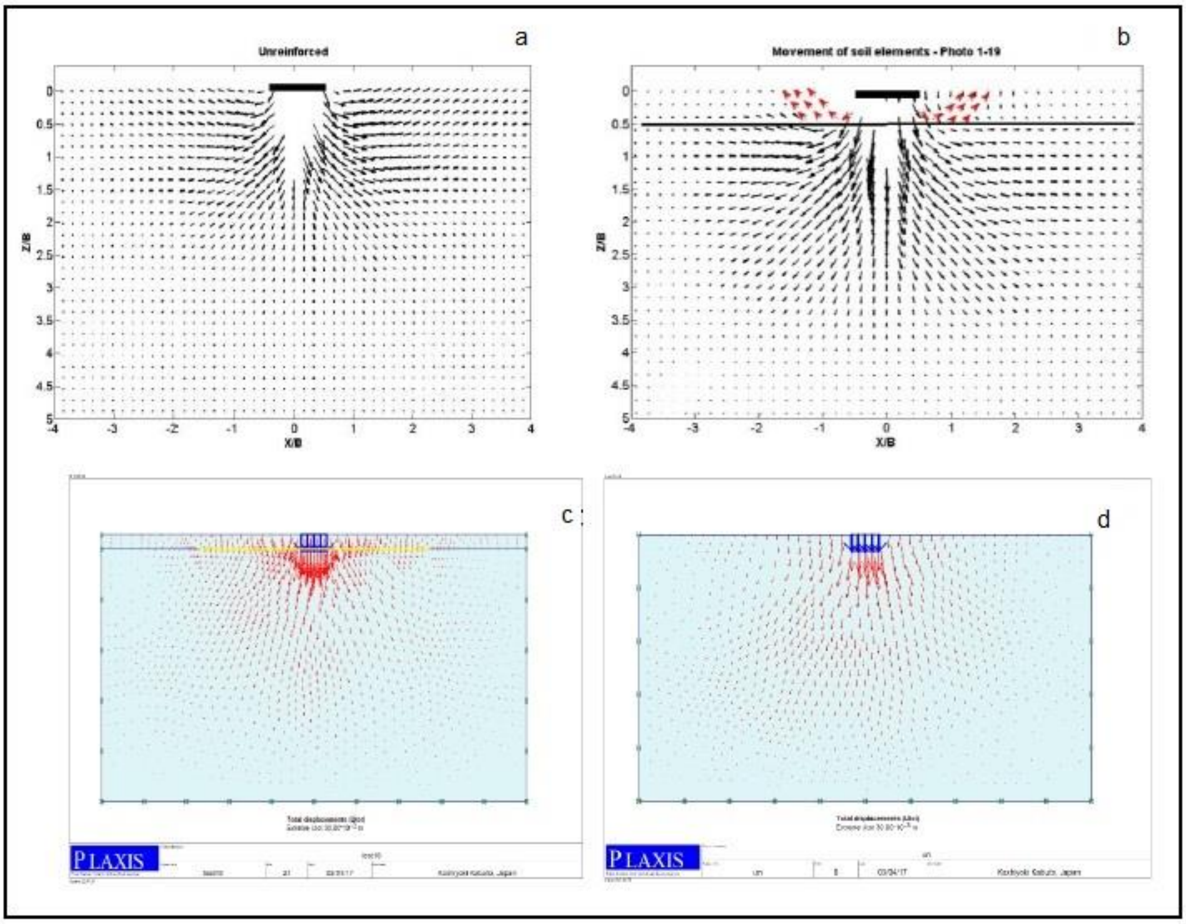

Figure 10. Failure surfaces in unreinforced soil and soil reinforced with one layer at a settlement of (S/B = 0.5) in experimental and numerical models.

4. Conclusion

A laboratory and numerical model were developed in this study to evaluate the bearing capacity of a strip footing on a sandy soil bed. Considering the limitations of the experimental model and the influence of the size and parameters of the model on the results, the following conclusions can be drawn regarding the application of reinforcements in sandy soils for strip footing performance:

The experimental and numerical models demonstrated that the application of reinforcements in sandy soil significantly improves the bearing capacity of strip footings.

4.1. For Reinforced Soil at Depth

The failure surface in reinforced soil exhibits a deeper and larger failure zone compared to the unreinforced soil. This is consistent with the proposed bearing capacity theory.

4.2. Reinforcement Selection and Bearing Capacity

For improved performance and higher bearing capacity, the use of geogrid reinforcement has shown significant effectiveness. In the experimental and numerical models, the use of geogrids resulted in an approximately 2.1 times increase in bearing capacity in the laboratory model and 1.79 times in the numerical model.

4.3. Effect of Reinforcement Number

In this study, an increase in the number of reinforcements led to a further enhancement in bearing capacity. The results showed that using two layers of reinforcement increased the bearing capacity ratio by 2.27 times in the experimental model and by 2.09 times in the numerical model compared to a single layer of reinforcement.

4.4. Consistence Between Experimental and Numerical Results

The results from the experimental and numerical models show reasonable agreement, although the numerical model yields lower values compared to the experimental model. This discrepancy may arise from the differences in soil behavior and reinforcement interaction between the two models. The laboratory model assumed a plane-strain condition, which might explain the observed differences, with the laboratory model showing reduced shear effects along the boundary.

4.5. Comparison of Numerical and Physical Models

For a more comprehensive comparison, the relative errors in pressure and settlement parameters were calculated. The relative errors were smaller in the numerical model, indicating a more accurate representation of the soil-reinforcement behavior in the numerical model. The relative error is defined as:

Relative Error = $|yi - yj| / yi$ (1)

The relative errors for all parameters in the experiments are provided in Table 4.

Table 4. Relative Error Percentage for Experimental Data

Test Number	Relative Error (%)
1	9
2	15
3	16
4	15
5	11
6	11
7	15
8	12
9	10
10	11

The relative error percentages in the results show that the values obtained are close to the actual values, which are derived from the experimental results.

This study was conducted using a scaled model compared to the actual model. Given the different materials used, the behavior of the soil and reinforcement may not perfectly represent the real-world conditions. Therefore, for accurate results, scaling to larger models should be considered. In this study, the behavior of soil and reinforcement was thoroughly investigated, and the influence of reinforcement type was also assessed.

References

[1]. Movahedan, M. 2012. Application and water leakage control of geomembrane linings in water reservoirs. Appl. Res. Irrig. Drain. Struct. Eng. 13(3): 15-28. (in Persian)

[2]. Huang, C. C. and Menq, F. Y. 1997. Deep footing and wide-slab effects on reinforced sandy ground. J. Geotech. Geoenviron. Eng. ASCE 123 (1): 30-36.

[3]. Huang, X., & Tatsuoka, F. 2020. Bearing capacity of strip footing built on geogrid-reinforced sand over soft clay slope and subjected to a vertical load. Electronic Journal of Structural Engineering, 19(1), 24-35.

[4]. Yamamoto, K. 1998. Failure mechanism of reinforced foundation ground and its bearing capacity analysis. Ph. D. Thesis. Kumamoto University, Japan.

[5]. Moghaddas-Tafreshi, S. N. and Dowson, A. R. 2010. Comparison of bearing capacity of a strip footing on sand with geocell and with planar forms of geotextile reinforcement. J. Geotext. Geomembranes. 28(1): 72-84.

[6]. Qiming, C. and Murad, A. F. 2015. Ultimate bearing capacity analysis of strip footings on reinforced soil foundation. 55(1): 74-85.

[7]. Qiming, C. and Murad, A. F. 2024. Seismic Bearing Capacity of Strip Footings on Reinforced Soil Foundations. Geotechnical and Geological Engineering, 52(4): 612–630. DOI: 10.1007/s11041-024-00968-3

[8]. Hajialilue-Bonab, M., Katebi, H. and Behroz-Sarand, F. 2012. Behavior Investigation of Reinforced and Unreinforced Sand below Strip Foundation using PIV. Cinil Eng. J. 23(2): 103-114. (in Persian)

[9]. Ranjan, R., Raviteja, S., Singh, H., & Patel, J. B. (2024). A Comprehensive Finite Element and Reliability-Based Analysis of Hybrid Reinforced Earth Retaining Wall Stability and Deformation. Transportation Infrastructure Geotechnology, 12(1), 41. https://doi.org/10.1007/s40515-024-00488-2

[10]. Lin, Z., Yan, C., Sang, B., et al. 2024. Strain characteristics of reinforced soft clay around tunnel under metro loads. Discover Applied Sciences, 6: 389. https://doi.org/10.1007/s42452-024-06090-y

[11]. Khawaja, L., Asif, U., Onyelowe, K., Al Asmari, A. F., Khan, D., Javed, M. F., & Alabduljabbar, H. (2024). Development of machine learning models for forecasting the strength of resilient modules of subgrade soil: genetic and artificial neural network approaches. Scientific Reports, 14, 18244. https://doi.org/10.1038/s41598-024-69316-4

[12]. Guido, V. A., Chang, D. K. and Sweeney, M. A. 1986. Comparison of geogrid and geotextile reinforced earth slabs. Can. Geotech. J. 23, 435-440.

Management and Planning Without Overflowing from the Riverbed

Hüseyin Emre SÜME(*1) **Gülay BOZ**(2)

(1) Recep Tayyip Erdoğan University, Faculty of Engineering, Department of Civil Engineering, Rize, Türkiye

(2) Recep Tayyip Erdoğan University, Faculty of Engineering, Department of Civil Engineering, Rize, Türkiye

Received date**: 29.05.2025**; Accepted date**: 16.06.2025**; Published date: **28.06.2025**

Turkish Journal of Hydraulic, Vol : **9**, Number : **1**, Page : **16-24**, **(2025)**

e-ISSN: **2636-8382**

SLOI: http://www.dergipark.org.tr

*Corresponding author e-mail: hüseyinemre_sume25@erdogan.edu.tr

Abstract
Precautions taken to reduce risks before floods occur play a critical role in minimizing loss of life and property. Throughout history, civilizations have emerged and developed on river banks. In the development of these civilizations, streams have played a role in meeting the needs of drinking and utility water for settlements, irrigation water for agricultural areas, and, in later years, energy and industry. In recent years, floods have begun to occur due to changes in precipitation due to global climate change. The first step in this process is to determine areas at risk of flooding using scientific methods. Preparation of risk maps, limiting construction in these areas, and making appropriate land use plans are basic approaches. For structural design, it is important to estimate the magnitude of floods and the effects and efficiency of these structures on flood waves. For this purpose, cooperation should be established between local governments, central authorities, and relevant institutions, flood early warning systems should be established, and the public should be informed about these systems. In addition, flood-resistant infrastructure projects (such as sewer systems, flood dams, and stream rehabilitation) should be planned and implemented in advance. The society should be prepared for floods through education and awareness activities, and organizational preparation should be increased through pre-disaster drills. This study focuses on the definition of flood, types of floods, classification of floods, flood diversion, and flood protection principles, and aims to create public awareness.

Keywords: *Flood, Flood Control, Flood Mitigation, Climate Change*

1. INTRODUCTION

One of the most common natural disasters experienced across many countries worldwide is flooding, which occurs when a body of water exceeds its usual volume and river levels rise above their annual average. Humanity has been implementing various measures for centuries to protect itself from this disaster. Nevertheless, each year, hundreds of thousands of people lose their lives, become homeless, and suffer severe economic losses. In recent years, increases in temperature and precipitation values have been observed due to global warming. Especially when precipitation exceeds normal levels, it often leads to sudden flash floods.

In our country, flooding ranks second only to earthquakes among natural disasters and is not a phenomenon that can be fully controlled. Therefore, the aim of the measures taken is not to prevent floods entirely but to minimize their adverse impacts. Since its establishment in 1953, the General Directorate of State Hydraulic Works (DSİ) has been developing and implementing various projects to protect the country's water resources. Numerous structures have been constructed to control and mitigate the effects of flooding. These include dams, flood detention basins, flood diversion channels, and streambed rehabilitation works. However, it is also essential that other institutions in the region show sensitivity and cooperate with these efforts.

What is a flood, and why does it occur? A flood is the overflowing of a river from its bed or the inundation of inhabited or uninhabited land due to rising water levels from various causes. Despite today's accumulated scientific knowledge, floods—whether caused by natural processes or human intervention—continue to pose serious threats in our country and many parts of the world. Fundamentally, floods are natural events. However, it is predominantly human interference that transforms this natural phenomenon into a disaster with potential for loss of life and property.

The causes of floods can be categorized into two main dimensions: Natural causes: In many regions of the world today, precipitation levels have significantly exceeded long-term averages. Anthropogenic causes: Any human activity that is incompatible with nature or obstructive to natural systems increases the potential damage caused by floods and thus turns flooding into a disaster [1-4].

2. CAUSES OF FLOODS AND FLOOD FORECASTING

In flood forecasting, it is essential to process hydrometeorological data in accordance with hydrological principles and to consider qualitative information in the form of expert opinion. The underlying causes must be thoroughly examined, and preventive measures should be taken based on the specific conditions under which floods occur.

2.1. Unexpected conditions

Natural Conditions:
Since it is not possible to intervene in natural conditions, taking preventive measures in this regard is generally not feasible. Intense rainfall, sudden snowmelt, or ice jams that lead to the narrowing of flow cross-sections are typical examples of such conditions.

Dam Failures:
Dam failures may occur due to various factors such as insufficient spillway capacity, poor foundation conditions, or the failure to connect the impermeable core to a suitably impermeable foundation layer, which can result in seepage from underneath the structure.

Tidal Events, Storms, and Earthquakes:
Events such as oceanic tides, severe storms, and earthquakes are beyond human control. However, some precautionary measures may be taken in advance to mitigate their possible impacts.

Geomorphological Conditions:
These conditions are related to the natural characteristics of river basins, and as such, human intervention is not applicable.

Human Interventions and Social Factors:
Improper land use, deforestation, destruction of vegetation, unauthorized settlements within riverbeds, and erosion are primarily anthropogenic factors. These conditions can be managed, and the damage caused by floods can be minimized through appropriate mitigation measures. Additionally, heavy rainfall over a snow-covered river basin can result in rapid snowmelt, leading to severe flooding. Soil moisture levels during rainfall events also play a significant role in flood generation.

2.2. Meteorological Conditions

a) Winter Precipitation-Induced Floods:
Winter precipitation associated with well-developed westerly depressions and warm fronts is particularly influential in Central and Northern Europe. When the volume of precipitation is high, continuous, and prolonged, the soil becomes saturated, resulting in large volumes of surface runoff and subsequently, flooding.

b) Summer Convective Storm-Based Floods:
Convective storms triggered by significant temperature differences can produce extremely intense rainfall events, leading to severe and sudden flooding.

c) Temperature Contrast (Convective) Storm-Driven Floods:
Meteorological conditions frequently observed in Southeastern and Western Europe—including Turkey—often involve cold fronts interacting with convective systems.

These systems can move from the Mediterranean inland and result in extreme rainfall lasting more than 24 hours. This category includes snowmelt-induced floods, urban drainage overflows in densely populated areas, coastal storm surge and tidal floods, as well as floods caused by dam failures.

2.3. In Terms of Their Locations of Occurrence:

*River and stream floods
*Mountainous area floods
*Urban floods
*Coastal floods
*Fluvial (riverine) floods
*Storm surge inundation
*Seismic sea wave (tsunami) floods
*Flash floods
*Ice jam floods
*Debris or mudflows
*Groundwater-related flooding

3. DAMAGES OF FLOODS

Direct Damages:
These refer to visibly observable impacts such as structural collapse, mud deposition, scouring, and material displacement. Such damages are quantified based on the financial cost required for reconstruction or repair of affected areas.

Indirect Damages:
These include disruptions and losses in trade, economic activities, and public services due to flooding.

Non-Monetary Damages:
These are damages that cannot be expressed in monetary terms, such as loss of human life, health impacts, and threats to social and economic security. Efforts to study and mitigate flood damage began in the 20th century and have evolved through three successive phases:

Hydraulic Structures Phase (1930–1960):
In this period, infrastructure such as dams, retaining walls, levees, and diversion tunnels were constructed. Additionally, formulas and algorithms were developed to estimate flood peak discharges.

Floodplain Management Phase (1960–1980):
During this stage, measures such as early warning systems and land use planning were implemented to reduce flood risks.

Monitoring and Control of Flood Structures Phase:
This phase focuses on the operational management, inspection, and performance monitoring of existing flood protection structures to ensure their effectiveness and sustainability.

4. FLOOD MANAGEMENT

Flood management refers to the comprehensive set of planning, implementation, and response activities aimed at preventing flood risks, mitigating their impacts, and enhancing preparedness, particularly in areas surrounding rivers, streambeds, water resources, and coastal cities.

The primary objectives of flood management include preventing loss of life and property, reducing economic damages, minimizing environmental impacts, and ensuring sustainable water resource management.

4.1. Flood Management Process

A. Flood Risk Assessment
Collection of hydrological and meteorological data
Analysis of historical flood events
Mapping of high-risk areas (flood risk maps)

B. Preventive Measures
Stream rehabilitation and regulation of floodplains
Construction of dams, levees, and water storage structures
Integration of flood risk considerations into urban planning. Flood insurance schemes (e.g., TARSİM in Turkey)

C. Early Warning and Evacuation Systems
Meteorological alert systems
Emergency evacuation plans prepared by local authorities

D. Emergency Response During the Disaster
Search and rescue operations
Evacuation and first aid
Temporary shelter and food assistance

E. Post-Disaster Recovery
Damage assessment and compensation procedures
Infrastructure repair and restoration
Resettlement planning and post-disaster development strategies

4.2. Flood Management In Turkey

- The General Directorate of State Hydraulic Works (DSİ) is responsible for implementing flood protection projects.
- The Disaster and Emergency Management Authority (AFAD) includes flood hazards within its disaster management planning framework.
- Municipalities and Provincial Special Administrations are responsible for drainage and infrastructure planning at the local level.

The classification that should be taken into account in flood management, as proposed by Kenny (1990), is as follows.

Flood Damage Zone I (Direct Flood Zone):
Residential development should be prohibited in these areas. Only low-impact recreational uses, such as picnic areas, should be permitted.

Flood Damage Zone II (Areas with alluvial fans and natural channels shallower than 1 meter):
Very limited residential development may be allowed, and only in specific areas. Settlements should not be permitted within natural channels or valley floors.

Flood Damage Zone III (Disconnected upper and lower basin areas, low-lying terrains, and erosion/transport zones with slopes generally less than 2%):
Measures similar to those in Zone II should be implemented. Special attention should be paid to the design of culverts under roads.

Flood Damage Zone IV (Areas with steep slopes, typically near mountainous regions in the upper parts of catchments, featuring valleys that are largely disconnected):
Bridges, roads, and culverts should be designed to accommodate both floodwaters and boulders larger than 1 meter in diameter. Limited residential development may be permitted in flatter sections of these areas.

5. PRINCIPLES OF FLOOD PROTECTION

5.1. Planning Stage

In the planning phase, the design flood and the flood characteristics of the region are identified, along with the area to be protected. Applicable methods and protection measures are determined, and the cost and effectiveness of each measure in flood control are assessed. The optimal solution is selected based on achieving maximum benefit at minimum cost. An economic analysis is then conducted by comparing the costs and expected benefits of the proposed flood protection measures.

Flood calculations, particularly in the fields of hydraulics are significant subject in the field of engineering. These calculations are conducted to estimate the magnitude, frequency, and potential impacts of floods that may occur in a given region. Typically, they serve the following purposes:

- To assess flood risks
- To design structures such as dams, culverts, and bridges
- To plan residential and urban development areas
- To develop early warning systems

Key components include:
a. Hydrological Analysis:
Precipitation data: Maximum daily/hourly rainfall amounts.
Flood frequency analysis: Flood magnitudes and return periods are estimated using statistical distributions such as Gumbel and Log-Pearson Type III (e.g., 100-year flood).

b. Hydraulic Modeling:
Flow calculations: Discharge (Q) = Cross-sectional Area (A) × Flow Velocity (V). River channel capacity and flood extent: Water surface elevations and flood-prone areas are determined using software tools like HEC-RAS.

c. Topography and Soil Data:
Factors such as digital elevation models (DEM), soil permeability, and vegetation cover influence flood behavior.

d. Flood Frequency and Return Period (T):
For example, if a discharge of 550 m^3/s is expected to occur once every 100 years in a specific region, the annual probability of such a flood is $P = 1/T = 1/100 = 0.01$, or 1%.
Alternatively, if the same discharge occurs every 50 years, the annual probability would be $P = 1/T = 1/50 = 0.02$, indicating a 2% chance of occurrence in any given year [5-9].

6. FLOOD CONTROL AND MITIGATION METHODS

For design flood assessments, the General Directorate of State Hydraulic Works (DSİ) uses recurrence intervals of 10, 50, and 100 years in small-scale flood hydrology projects such as detention basins, flood protection, and diversion channels. For larger structures, depending on the size of the facility and downstream conditions, design floods with return periods of 500 and 1000 years may also be considered.

In cases where the total storage volume is large, flood hydrographs are generated. For small-volume storage reservoirs ($\leq 10^6$ m^3), 100- or 500-year floods are used; for large-volume reservoirs ($>10^6$ m^3), if there is no or low risk to human life, 500- or 1000-year floods are considered; and in cases where there is a high risk to human life in large-volume reservoirs, risk analyses are carried out based on 10,000-year flood events.

The recurrence intervals for different types of structures are as follows: Earth-fill dams: 15,000 years; Rock-fill dams: 10,000 years; Concrete dams: 1,000 years; Levees near urban areas: 250 years; Levees in rural or remote areas: 100 years; Cofferdams: 25 years.

6.1. Flood Routing

Flood routing calculations offer numerous advantages in terms of flood control. When the magnitude of a flood is known at a specific location along a river, flood routing techniques can be used to estimate the flood magnitude at downstream locations many kilometers away several hours or even days in advance. Since flood routing enables the estimation of changes in discharge and water level along the river course, it provides a reliable basis for determining the dimensions of flood protection structures, such as levees. In the case of reservoirs, if the inflow flood hydrograph is known, flood routing allows the calculation of outflow discharges through spillways. This makes it possible to design the dimensions of spillways, determine cofferdam heights, estimate the maximum water level in the reservoir, and define both the height of the dam and the extent and duration of land submergence below the dam.In urban stormwater drainage systems, flood routing is used to model how a flood wave propagates through the network after intense rainfall. This helps identify which parts of the city are likely to be inundated.

By applying flood routing in reservoirs, the outflow discharges through spillways can be determined based on the inflow hydrograph. As a result, the appropriate dimensions of spillways, the required height of cofferdams, the peak reservoir water level, the height of the dam, and the extent and duration of submergence of land beneath the reservoir can all be accurately assessed. Similarly, in stormwater collection networks, flood routing enables the analysis of flood wave propagation through the system, which can be used to identify areas of potential urban flooding.

6.2. Non-structured Flood Control

For effective non-structural flood control, the following measures should be implemented:

- Developing a floodplain management plan and identifying flood risk levels,
- Establishing shelters or designated safe areas above projected flood levels for humans and animals,
- Installing flood forecasting and early warning systems,
- Planning rescue operations and ensuring effective flood response during events,
- Temporarily evacuating flood-prone areas when necessary,
- Prioritizing and completing critical activities in flood-prone areas before the flood season,
- Obtaining flood insurance coverage.

6.3. Structured Flood Control

For structural flood control, the following measures should be considered:

- Reducing flood runoff through soil conservation and watershed management practices,
- Regulating river channels by lowering the riverbed or increasing flow velocities within the cross-section to reduce floodwater levels,
- Diverting floodwaters using flood diversion channels or spillways,
- Attenuating peak flood discharges by temporarily storing part of the floodwater in detention basins, flood detention reservoirs, or dams,
- Containing flood flows within a designated floodway using levees, flood walls, or closed conduits [10-16].

7. FLOOD PROTECTION STRUCTURES

7.1. River Channel Regulation

By regulating the river channel, it is possible to reduce the harmful impacts of flooding by increasing the discharge capacity that the riverbed can convey above a certain water level. Widening or deepening the river channel is a feasible method, particularly for small rivers with channel widths up to 30–40 meters (Figure 1).

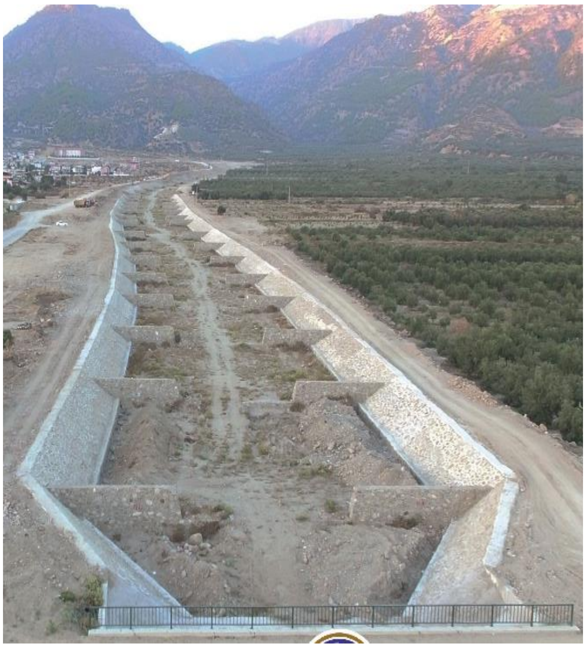

Figure 1. Rivel Channel Modification [17].

7.2. Flood Channel

In certain sections of a river where it is not feasible or advisable to modify the entire riverbed to convey all floodwaters, or where levee construction is impractical, a portion of the floodwater can be diverted into a flood diversion channel to reduce the flood load on the main river.

Where topographic conditions are favorable, the river may be transformed into a lake, or natural lakes can be modified to function as flood diversion channels (Figures 2 and 3).

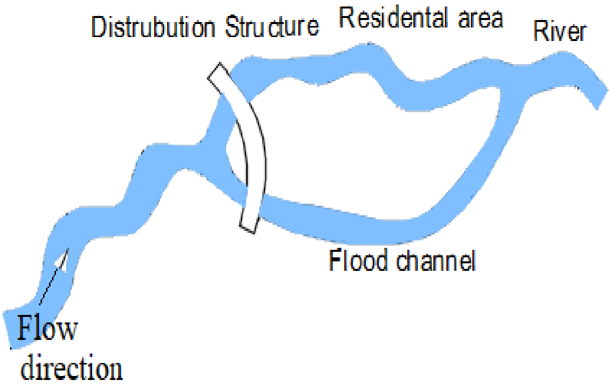

Figure 2. Flood Channel (A)

Flood detention basins are single-purpose flood control structures with non-regulated outlet systems, unlike dams and levees. These basins temporarily store floodwaters and release them back into the river channel in a delayed manner, at flow rates that do not pose a threat. In this way, the peak discharges of the flood hydrograph are reduced. Detention basins are typically located away from the main river channel and are characterized by large surface areas and shallow depths. Outside of the flood season, they can also be utilized as agricultural land. In terms of their impact on downstream flows:

Flood detention basins can be implemented in various configurations, such as:

- Basins designed without any river regulation,
- Basins planned in combination with partial river regulation measures,
- Basins constructed specifically to retain only extreme (maximum) flood events.

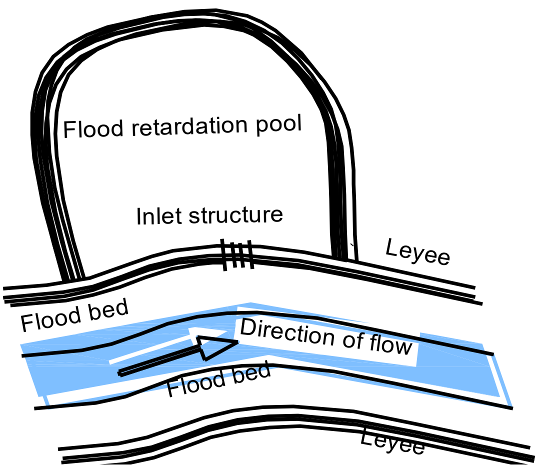

Figure 2. Flood Channel (B)

7.3. Flood Trap

These are small dams, typically ranging in height from 10 to 20 meters, designed to temporarily retain floodwaters and thereby reduce peak flood discharges in downstream areas. They are generally constructed without gates, and one or more bottom outlets function as uncontrolled discharge structures, which are kept continuously open.

The maximum capacity of a debris retention basin is defined by the maximum water level within the reservoir and is limited by the discharge that can be safely conveyed by the downstream river channel (Figure 4).

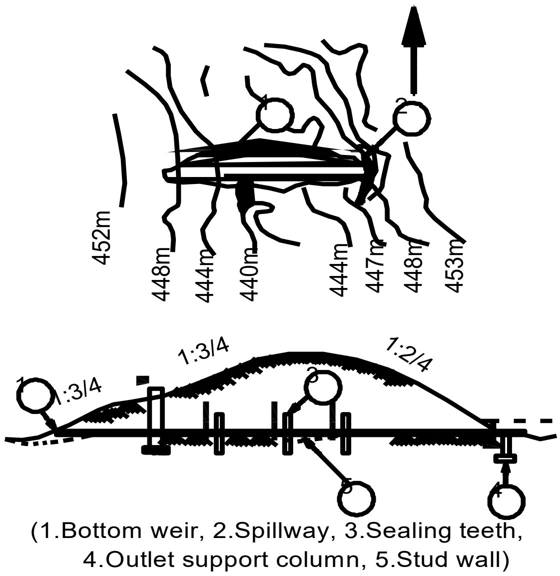

Figure 3. Flood Trap

7.4. Levees

A levee is an artificial embankment constructed along a river channel, either on the riverbed or along the banks, to prevent erosion and to contain floodwaters within the cross-section of the river.

Levees can be classified as follows:

- Closed Levee: A levee that does not allow floodwaters to overtop from either the upstream or downstream sides.
- Open Levee: A levee connected to a higher elevation on the upstream side to prevent overtopping, while the downstream end remains open, allowing floodwaters to enter the protected area.
- Backwater Levee: A levee extended along tributary streams to the point where the backwater effect from the main river is no longer felt.
- Transverse Levee: A levee constructed perpendicular to the river to divide the protected

area into compartments, minimizing damage in the event of levee failure.

- Ring Levee (Encircling Levee): A levee that encloses specific areas to protect them from flooding.
- Seepage Levee: A secondary levee intended to stop seepage from the main levee.
- Relict Levee (Redundant Levee): An older levee that has been replaced by a new one but is retained as an additional safety measure.
- Wing Levee: A levee constructed to alter the direction of floodwater flow (Figure 5).

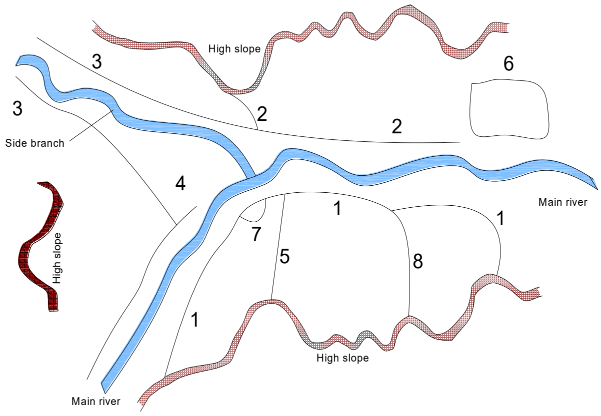

Figure 5. Classification of Levees

In some cases, levees are further classified as follows:

- Summer Levee: A levee designed to protect agricultural lands from flooding only during the plant growth season.
- Winter Levee: A levee whose crest is planned 0.5 to 1.2 meters above the maximum flood level. This is referred to as the main levee, and its implementation is considered complete levee protection.
- Contiguous Levee: A levee whose inner slope is a direct continuation of the riverbank surface, with no designated floodplain between the levee and the river channel (Figure 5).
- Detached Levee: A levee designed with a designated floodplain between the river channel and the levee itself (Figure 6).

Potential Negative Effects of Levee Construction:

- Although levees are essential for flood protection, in some cases they may lead to adverse effects on river dynamics and surrounding environments:
- The natural retention of floodwaters within the valley is eliminated.
- Water levels within the river channel may rise.
- The peak discharge of flood waves may increase.
- Flow velocity and shear stress within the floodplain can intensify.
- Agricultural lands may be deprived of nutrient-rich sediments (silt).
- Groundwater recharge from flood flows may be reduced, leading to decreased base flows.
- Sediment deposition may occur in wider floodplain areas.
- Accumulated sediments can elevate floodwater levels, eventually necessitating the raising or upgrading of existing levees.

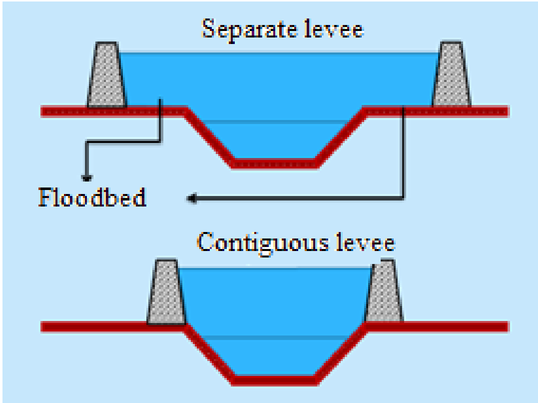

Figure 6. Contiguous (Top) and Detached Levee (Bottom) on floodplain

Separate levee
Contiguous levee
Floodbed
In general, levees are designed with a trapezoidal cross-section and constructed using homogeneous earth fill. The dimensions of the levee vary depending on its intended purpose, the characteristics of the foundation soil, and the properties of the fill material used (Figure 7).

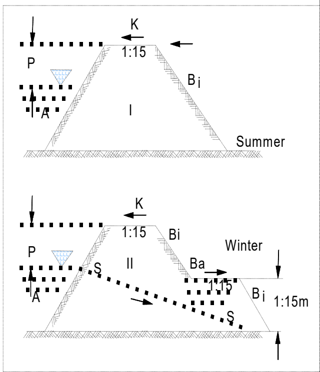

	Symbol	Winter bank	Summer bank
Inner slope	A	1/2-1/4	1/3-1/4
Outer slope	Bi	1/1.5-1/2	1/5-1/10
Crest widthi (m)	K	2.5-4.0	1-2
Free board	P	0.5-1.2	0.3-0.6
Shoulder	Bi	3.5-4.0	-
İnfiltration line slope	S	1/5-1/8	1/3-1/5

Figure 7. Design Criteria for Levee

Levees are generally designed based on floods with a 50-year return period. To prevent damage during larger flood events, special emergency spillways are provided at appropriate locations. The slope along the levee alignment is selected to match the water surface slope of the river during flood conditions (Figure 8).

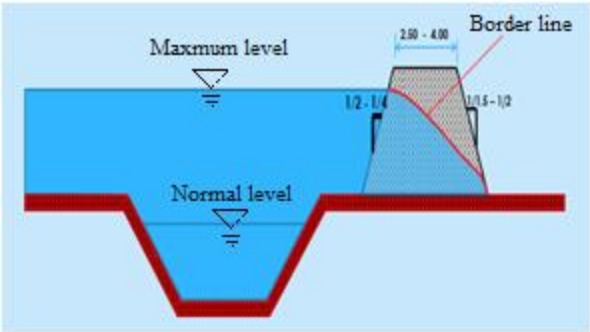

Figure 8. Levee Design

The seepage line within the embankment is the primary factor in determining levee dimensions. If the seepage line extends outside the levee, a berm on the outer slope or a permeable toe drain made of high-permeability material may be considered.

In cases where the levee fill material is highly permeable, impermeability can be ensured by applying a surface lining on the outer face or by incorporating a central impermeable core. To collect and safely discharge seepage water, a drainage ditch parallel to the levee is recommended.

Common failure mechanisms in levees include:

- Overtopping,
- Piping,
- Saturation of the embankment,
- Foundation erosion, and
- Slope instability on the outer faces (Figure 9).
-

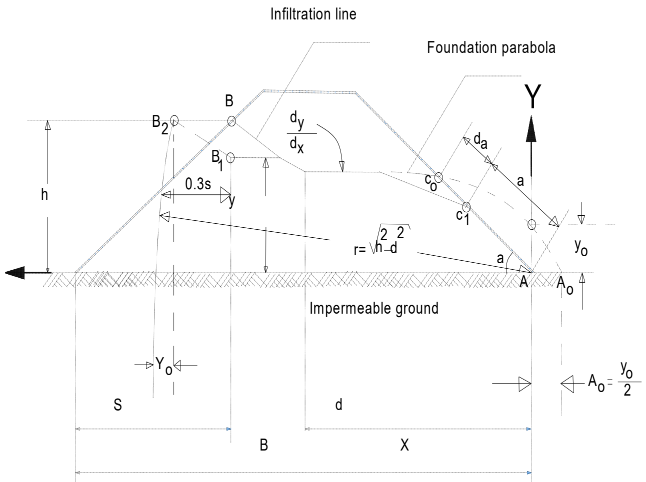

Figure 9. Seepage in Levees

In densely populated areas where land is highly valuable, flood walls are constructed along river corridors to confine floodwaters within the channel (Figure 10).

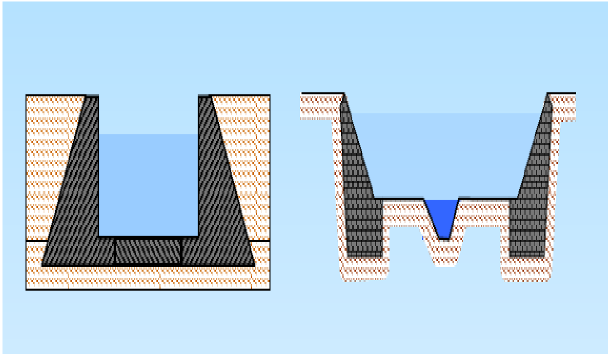

Figure 10. Flood wall

8. Conclusion and Recommendations

Due to the rapidly changing socio-economic structures around the world, the necessity of addressing flood risks has become increasingly evident. In the design of flood protection structures, it is crucial to understand the flood characteristics of rivers, particularly during the planning of economic analyses, flood damage assessments, and zoning regulations. Identifying the regions where flood protection structures are most needed allows for the implementation of necessary precautions before any loss of life or property occurs.

The design of flood protection or control structures requires careful consideration of river gradient, geological investigations, discharge capacity, and cross-sectional characteristics. The type of construction materials to be used should be selected to maximize cost-effectiveness. In Turkey, flood protection works carried out by the State Hydraulic Works (DSİ) are implemented both in urban and rural areas. These projects are often designed to enhance agricultural land use and to create landscape areas. However, it has been observed that such developments can have negative impacts on natural ecosystems. Therefore, it is essential that these projects are implemented appropriately and in a manner that minimizes harm to the environment.
Moreover, special attention should be paid to the following issues:

- Excavation waste and similar materials should not be dumped into streambeds.
- Instead of closed channels, open channels that are easier to clean and maintain should be constructed.
- Residential areas should not be developed in low-lying or depressed regions near rivers, canals, or streambeds; zoning plans must be implemented based on flood recurrence discharges.
- Forested areas should be expanded, land should be terraced, and afforestation should be carried out to reduce runoff and soil erosion.

- Check dams, reservoirs, or retention ponds should be constructed on rivers to capture sediment.
- Necessary infrastructure should be developed for the diversion of excess water.
- Underground sewer and wastewater drainage systems should be built with large capacity, and their outlets should not discharge directly into seas or river basins.
- Drainage systems should be installed on roads, streets, and bridges to prevent water accumulation.

As with earthquake preparedness, a state of alert and readiness must be maintained. Emergency response teams should be equipped with an adequate number of water pumps, vacuum trucks, and rescue boats, and comprehensive intervention scenarios should be developed in advance.

References

[1] Kerim, A., & Süme, V. (2019). Floods and flood protection structures. Turkish Journal of Hydraulics, 3(1), 1–13.

[2] Yüksek, Ö., Babacan, H. T., & Yüksek, O. (2022). Causes, damages, and flood management practices in the Eastern Black Sea Basin. Turkish Journal of Hydraulics, 6(2), 36–46.

[3] Yerdelen, C., Engin, U., & Eriş, E. (2023). Flood risk analysis with prevention scenarios for Zeytinli Stream. Turkish Journal of Hydraulics, 7(2), 22–29.

[4] Daneshfaraz, R., Zirei, B., Ebadzadeh, P., Abbaszadeh, H., & Mosavi, B. (2024). Experimental investigation of the effect of a contracted section at the downstream of a rectangular channel on energy dissipation. Turkish Journal of Hydraulics, 8(1), 1–6.

[5] Babacan, H. T. (2022). Development of a flow prediction model for Aksu Stream using machine learning. Turkish Journal of Hydraulics, 6(1), 1–11.

[6] Akman, M. U. (2021). Evaluation of flood protection and control structures. Turkish Journal of Hydraulics, 5(1), 25–31.

[7] Ateş, H., & Yıldız, O. (2023). Experimental and numerical investigation of hydraulic jump under gate. Turkish Journal of Hydraulics, 7(2), 1–14.

[8] Alashan, S. (2023). Pressure intensity coefficient. Turkish Journal of Hydraulics, 7(2), 15–21.

[9] Üçüncü, O. (2022). Urban Hydrology: Urban Drainage Conditions According to Turkish Rainwater Collection and Disposal Regulation. Turkish Journal of Hydraulics, 6(2), 1–13.

[10] Börü, S., & Toprak, Z. F. (2022). Comparison of Environmental Impact Assessment Processes for Hydropower Plants. Turkish Journal of Hydraulics, 5(2), 42–50.

[11] Daneshfaraz, R., Abbaszadeh, H., & Aminvash, E. (2022). Theoretical and Numerical Analysis of the Applicability of Elliptical Cross-Sections on Energy Dissipation of Hydraulic Jump. Turkish Journal of Hydraulics, 6(2), 22–35.

[12] Mutluay. E., (2019), Yüksek Lisans Tezi, Sel Risk Yönetimi Kavramının Değişen Çerçevesi ve Mekansal Planlama ile İlişkisinin İncelenmesi: Edirne Örneği, İTÜ. FBE, İstanbul.

[13] .88785 A Model Proposal for the Flood Risk Analysis of the Architectural Heritage: Edirne Bayezid II Complex Flood Risk Analysis

[14] Erdoğan, B.G., Gül Ünal, Z., (2021), (A Model Proposal for the Flood Risk Analysis of the Architectural Heritage: Edirne Bayezid II Complex Flood Risk Analysis), MEGARON 2021;16(3):367-384,
DOI: 10.14744/MEGARON.2021.88785

[15] Oyanık M. & Cengiz E. (2020). (Disaster Consciousness and Belief in Fate: Gümüşhane Example), Afet bilinci ve kader ilişkisi: Gümüşhane örneği, The Journal of International Scientific Researches, 5(AI), 87-101.

[16] Bahadır, H., Reyhan Uçku, R., (2018), (Disasters in the Republic of Turkey According to the International Disaster Database), Uluslararası Acil Durum Veri Tabanına Göre Türkiye Cumhuriyeti Tarihindeki Afetler, Artvin Çoruh University Natural Hazards Application and Research Center, Journal of Natural Hazards and Environment

[17] Buharkent Municipality, River Management Project, Aydın. URL: https://www.google.com/search?q=buharkent+belediyesi&oq=buharkent+belediyes&gs_lcrp=EgZjaHJvbWUqCggAEAAY4wIYgAQyCggAEAAY4wIYgAQyDQgBEC4YrwEYxwEYgAQyBggCEEUYOTIHCAMQABiABDIHCAQQABiABDIHCAUQABiABDIICAYQABgWGB4yCAgHEAAYFhgeMggICBAAGBYYHjIICAkQABgWGB6oAgCwAgA&sourceid=chrome&ie=UTF-8

Flood Routing by the Muskingum Method and Neural Network

Marjan Moazamnia

Dept. of Civil Engineering, Faculty of Engineering, University of Bonab, Bonab, East Azerbaijan, Iran

Received date**: 03.05.2025**; Accepted date**: 29.05.2025**; Published date: **28.06.2025**

Turkish Journal of Hydraulic, Vol: **9**, Number : **1**, Page, **25-32**, **(2025)**

e-ISSN: **2636-8382**

SLOI: http://www.dergipark.org.tr

Corresponding author e-mail: m.moazamnia@ubonab.ac.ir

Abstract

Floods have consistently been one of the most significant natural disasters affecting humans. In a country like Iran, their impact is particularly pronounced due to the irregular patterns of rainfall both in space and time. Flood routing is a crucial aspect of hydraulic engineering, as it enables the prediction of how floods will rise and recede at specific points along a river. Various techniques and methods are employed to address routing problems. This Manuscript explores routing using Muskingum's method, the least squares error method, and neural networks. First, three proposed neural network models with different transfer functions were evaluated to identify the best-performing model. The results were then compared using the least squares method and validated against the model proposed by Choudhury and Sankarasubramanian (2009). Ultimately, both models yielded acceptable results; however, considering the RMSE values, the least squares error method's results are closer to those proposed by Choudhury and Sankarasubramanian (2009).

Keywords: *Flood routing, Muskingum, Least Squares Error, Neural Network, Transfer Function*

1. INTRODUCTION

Flood flow in a channel refers to the movement of a wave, making it crucial for engineers to accurately predict how flood levels will rise and fall at specific locations along the channel. Flood routing involves a series of operations that use the known upstream flow hydrograph to determine the downstream flow hydrograph. In other words, computational operations for analyzing flood patterns in streams (channels and rivers) involve predicting changes in hydraulic variables, flow geometry, and flood waveforms overtime at one or more points along the stream (Mirzazade, 2013). Using routing techniques and a single-point flood hydrograph, the desired flood height can be determined at any location along the river's course. Various hydraulic and hydrological methods are available to route floods. If data and statistics of output sections are not needed, hydraulic methods can be used, where output data is obtained through hydraulic routing at any section. Flood routing by hydrological methods is relatively simple and reasonably accurate but requires multiple inflow and outflow hydrograph data.

The most common river routing method is the Muskingum method. This method was first developed by McCarthy for flood control studies of the Muskingum River basin in Ohio in 1938. This method uses the continuity equation to perform river routing. Perumal (1994) derived the Muskingum method with variable parameters for flood wave routing in fixed-section channels directly from the Saint-Venant equations by assuming a constant water level gradient along a small span of the channel and establishing a steady flow between the depth in the middle of the span and the discharge at a section downstream. Mohan (1997) proposed a genetic algorithm for estimating the parameters of two nonlinear Muskingum methods.

This study compared the results of the proposed genetic algorithm with those obtained from nonlinear least squares and conjugate gradient regression methods. Unlike other techniques, the genetic algorithm does not require an initial estimation of parameters. The application of this method to the nonlinear relationship between storage and flow demonstrated that the genetic algorithm effectively estimates the parameters of the nonlinear model.

Al-Humoud and Esen (2006) used an approximate and straightforward method to determine the coefficients of the Muskingum method. This method is estimated based on calculating the slope of the inflow and outflow hydrographs at their junction. Chu and Chang (2009) used an adaptive inference system in the MATLAB environment to determine the flood trend using the Muskingum method. They compared the results obtained from the neural-fuzzy network with the genetic algorithm. They concluded that the values obtained from the fuzzy neural network can be used in the Muskingum method and have a better match with the observational data than other methods. Easa (2013) used the variable parameter method in flood routing. In his study, he used three flood hydrographs and considered the exponential parameter in the nonlinear Muskingum method as a variable. In his research, the exponential parameter changes with the amount of inflow. The inflow is divided into five parts, and a separate exponential parameter is considered for each part. Niazkar and Afzali (2014) used the modified Honey Bee Mating Optimization algorithm (HBMO) to find the parameters of the Muskingum method.

The primary advantage of this approach is its ability to quickly reach an optimal value across a wide range of parameters. Moghaddam et al. (2016) initially estimated the parameters of the nonlinear Muskingum method using Particle Swarm Optimization (PSO). They then applied this method to a new form of the four-parameter Muskingum method, utilizing three sample hydrographs and one real hydrograph from Iran. Their findings demonstrated that, although the new Muskingum method was more complex, it provided a better fit to the observational data, particularly for hydrographs with multiple flow peaks. katipoğlu and Sarıgöl (2023) for flood routing prediction applying empirical model decomposition (EMD) and neural networks. This study showed that the EMD model can improve the performance of machine learning models, and the EMD model was the most successful algorithm in flood routing computation. The aim of the study of Sari Sarıgöl (2024) is to compare the performance of machine learning, deep learning, and hybrid algorithms for flood routing prediction models in the Büyük Menderes River. In the research deep learning model Long-Short Term Memory (LSTM), machine learning model Artificial Neural Network (ANN), and hybrid machine learning models empirical mode decomposition (EMD)-ANN, and particle swarm optimization (PSO)-ANN algorithms were compared to forecast the flood routing results in two discharge observation stations in the Büyük Menderes river. The results showed that the hybrid algorithm PSO-ANN was the most successful in forecasting flood routing results among other models. In the present study, flood routing was performed using the Muskingum method by the least squares method and neural networks. There have been relatively limited studies in the field of reservoir routing using artificial intelligence models, and this is one of the innovations of the present article.

2. METHODOLOGY

2.1. Muskingum Method

Flood routing methods can be divided into hydraulic and hydrological. In hydraulic routing, the continuity equation and the equation of motion of unsteady flow are used, and in hydrological routing, which is a standard method in water engineering, the equation of motion is generally ignored, and the continuity equation for a control volume is used as follows:

$$I - O = \frac{ds}{dt} \tag{1}$$

Where I, O, and S are the inflow and outflow rates and the storage volume of the control volume, respectively. The governing relationship for the Muskingum method, which is obtained through the scaling curve equation, is in the form of Equation 2.

$$S = KO - KX(I - O) \tag{2}$$

In the equation above, K represents the reservoir coefficient, while X denotes the weight coefficient. The parameter K reflects the river's travel time, which is determined by the river's length and the speed of the flood wave. In contrast, X signifies the influence of flood inflows and outflows on the river's storage volume, typically varying between 0 and 0.5. By assessing these two parameters, it is possible to calculate the flood outflow hydrograph for each flood event in the river. The following equation (Equation 3) are utilized for this calculation:

$$O_{t+1} = C_1 I_t + C_2 I_{t+1} + C_3 O_t \tag{3}$$

Where I_t and I_{t+1} are the flood inflow discharges at times t and t+1 from the flood inflow hydrograph, respectively, O_t and O_{t+1} the flood outflow discharges at times t and t+1 (from the flood outflow hydrograph), C_1, C_2 and C_3 are the routing coefficients. These coefficients are determined from equations (4-6):

$$C_1 = \frac{Kx + 0.5\Delta t}{K(1-x) + 0.5\Delta t} \tag{4}$$

$$C_2 = \frac{0.5\Delta t - Kx}{K(1-x) + 0.5\Delta t} \tag{5}$$

$$C_3 = \frac{K - Kx - 0.5\Delta t}{K(1-x) + 0.5\Delta t} \tag{6}$$

Which Δt is the time step of the calculations. Equation (3) is used iteratively to calculate the outflow flood hydrograph by determining the trending coefficients.

2.2. Flood estimation model by Choudhury and Sankarasubramanian

The equation proposed by Choudhury and Sankarasubramanian (2009) is represented by equation (7):

$$C_1 \alpha I_t + C_3 \beta O_t = -(1 - C_1 - C_3) I_{t+\Delta t} \tag{7}$$

In this equation, c_1 and c_3 are Muskingum parameters and α and β are the upstream hydrograph evolution parameters, which are functions of the upstream watershed, river branch, and sudden change characteristics such as storms. The parameters c_1, c_3, α and β for a branch of the river are obtained by minimizing the objective functions (equations (8-11)).

$$f(1) = \min \sum_{t=1}^{N-1} \left(i_{t+1} - \overline{i_{t+1}}\right)^2 \tag{8}$$

$$f(2) = \min \sum_{t=1}^{N-1} \left(q_{t+1} - \overline{q_{t+1}}\right)^2 \tag{9}$$

$$f(3) = \min \sum_{t=1}^{N-2} \left(i_{t+2} - \overline{i_{t+2}}\right)^2 \tag{10}$$

$$f(4) = \min \sum_{t=1}^{N-2} \left(q_{t+2} - \overline{q_{t+2}}\right)^2 \tag{11}$$

In the equations mentioned above, i and q represents the predicted flow in the upstream section, while $\bar{i}$ and $\bar{q}$ denotes the predicted flow in the downstream section. These correspond to the observed inflow and outflow values, respectively. The Muskingum parameters have been derived by minimizing these equations. When used for prediction in two future time steps, the obtained parameters will have prediction errors due to measurement and estimation errors. The error at time t+2 may be present in the error terms at time t+1. To estimate the possible error at the next time step during the flow predictions, two other objective functions are formed as given in equations 12 and 13.

$$f(5) = \min \sum_{t=1}^{N-2} \left(E_{t+2}^{i} - \theta^{i} E_{t+1}^{i}\right)^2 \tag{12}$$

$$f(6) = \min \sum_{t=1}^{N-2} \left(E_{t+2}^{q} - \theta^{q} E_{t+1}^{q}\right)^2 \tag{13}$$

In the above equation, E is the error indicator and θ is the parameter that defines the propagation of the error. The optimal estimation of parameters θ^i and θ^q defines a linear relation between the error at times t+1 and t+2 for the upstream and downstream stations, respectively. Minimizing the six objective functions mentioned (Equations 8 to 13) makes it possible to estimate the model parameters and the error. With the parameter values obtained for the river branch, the model may be used for long-range prediction of the upstream and downstream stations.

2.3. Least Squares Error Method

This method minimizes the difference between the observed and estimated storage. Therefore, we formulate and minimize the error function in the following form.

$$E = \sum_j \left[AI_j + BO_j + S_1 - S_j\right] \tag{14}$$

Where A=KX, B=K(1-X), S_1 is the initial storage, and S_j is the observed relative storage at the jth time step. N is the number of observed values of inflow, outflow, and relative storage for the period under study in the river (Choudhury and Sankarasubramanian (2009)). After taking the derivative of the error equation and setting it equal to zero, the error function reaches its minimum value. The values of A and B will be obtained by solving the matrix form of equation 15:

$$\begin{bmatrix} \sum I_j^2 & \sum I_j O_j \\ \sum I_j O_j & \sum O_j^2 \end{bmatrix} \times \begin{bmatrix} A \\ B \end{bmatrix} = \begin{bmatrix} \sum I_j S_j \\ \sum O_j S_j \end{bmatrix} \tag{15}$$

The least squares method calculations were performed using a program written in MATLAB. The values of X and K were obtained as 0.237 and 1.631, respectively. Finally, based on these calculated values, the output hydrograph was calculated, the results of which are presented in the following graphs.

2.4. Artificial neural network

The concept of artificial neural networks was first introduced by Frank Rosenblatt in 1962 and then in 1986 by Rommelhart and McClelland with the invention and presentation of the perceptron model, which is modeled after the neurons in the human brain and simulates the intracellular behavior of brain neurons through mathematical functions defined. The computational weights in the communication lines of artificial neurons play the role of synapses in natural neurons. The breadth and flexibility of neural networks have made them widely used in problems of a predictive nature.

The working process of a simple single-layer network is shown in Figure 1. The following simple network consists of one input and one neuron, and the role of the transfer function (denoted by f) is observed. The input p applied to the neuron is weighted by multiplying it by the weight w, and the result is used as an input to the transfer function f, and the final output is obtained. The bias input is a constant value of 1, a tunable parameter of the neurons, not an input, and its use in the MATLAB software toolbox is optional. The bias value is added to the product of w.p. The main idea of neural networks is that by changing the values of w and b, the network adopts a correct behavior or decision.

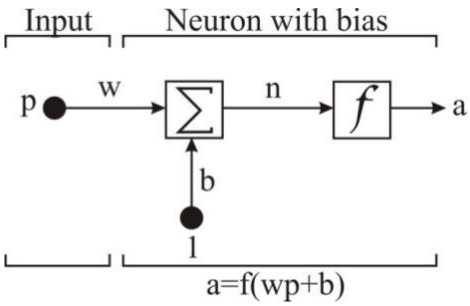

Figure 1. Structure of a single-layer neural network

A perceptron network has an input layer to apply inputs, a hidden layer, and an output layer to provide problem outputs. This type of network is usually trained using the backpropagation method. An example of this type of network is shown in Figure 2.

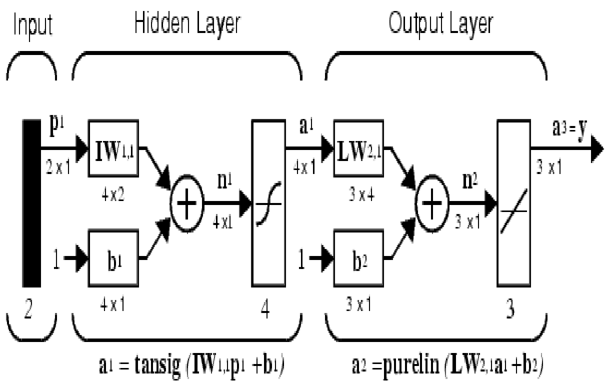

Figure 2. Structure of a multilayer perceptron with hidden neurons and output neurons with a linear function

The role of transfer functions in neural networks is to calculate the output of the layers from the input network. This review evaluated the performance of three different functions: logsig, tansig, and purelin. It is important to note that in multilayer networks, using the aforementioned transfer functions has been very common, but other transfer functions can also be used if desired. The diagram of these functions is given in Figure 3.

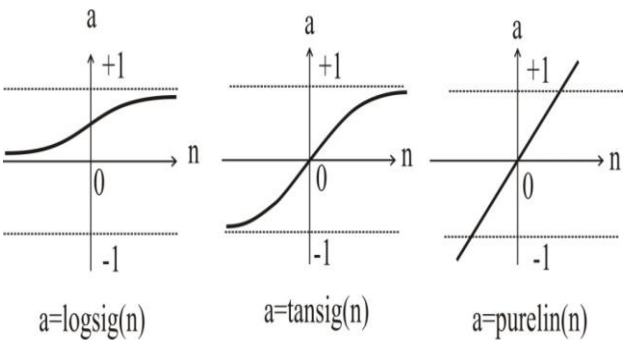

Figure 3. Diagram of transfer functions used in the neural network (Agami et al., 2009)

Given that the range of the tansig function is in the range of 1 and -1 and the range of the logsig function is in the range of 0 and 1, the input data is normalized to the smallest range, that the range of zero and one, using equation 16:

$$X_i' = \frac{X_i - X_{\min}}{X_{\max} - X_{\min}} \tag{16}$$

The goal of neural networks is to change the weight and bias matrix to reduce the error between the network output and the target values. In this paper, the normalized values of the inflow hydrograph are introduced as input, and the outflow hydrograph values are introduced as target data for simulation.

2.5. Data Availability

In this paper, the hydrograph from the data provided by Chow et al. (1988) has been routed using both neural networks and Muskingum's Method, employing the least squares error method. The results obtained from these approaches have been compared and presented alongside those from the study by Choudhury and Sankarasubramanian (2009). Additionally, the impact of the type of transfer function on the proposed neural network model has been examined. Table 1 and Figure 4 and 5 show data related to the hydrograph values of Chow et al. (1988) and the proposed model of Choudhury and Sankarasubramanian (2009).

Table 1 - Simulated data and values of the proposed model by Choudhury and Sankarasubramanian (2009)

Observational Hydrograph by Chow et al. (1988) (m^3/s)		The proposed model by Choudhury and Sankarasubramanian (2009) (m^3/s)			
		Flow model		Error model	
inflow	outflow	inflow	outflow	inflow	outflow
1.70	0.00	1.70	0.00	1.70	0.00
5.10	1.19	7.27	1.58	9.60	3.31
8.50	3.60	10.63	5.16	12.31	6.82
12.63	6.54	13.77	8.59	15.30	10.16
17.36	10.28	16.62	11.81	18.00	13.27
21.97	14.55	19.16	14.79	20.35	16.12
26.39	19.03	21.34	17.47	22.33	18.68
26.39	23.28	23.14	19.83	23.92	20.83
25.80	24.89	24.53	21.82	25.09	22.64
26.65	25.40	25.50	23.42	25.84	24.05
27.61	26.16	26.04	24.62	26.15	24.05
27.75	27.01	26.15	25.40	26.04	25.62
26.93	27.41	25.83	25.75	25.51	25.77
25.20	27.07	25.11	25.68	24.58	25.51
22.94	26.02	23.99	25.20	23.26	24.83
20.30	24.10	22.51	24.32	21.60	23.77
17.50	21.78	20.69	23.07	19.62	22.34
14.55	19.17	18.57	21.46	17.36	20.58
11.61	16.40	19.16	19.54	14.86	18.52
8.75	13.54	13.59	17.34	12.16	16.20
7.02	10.56	10.82	14.89	9.32	13.66
6.48	8.55	7.92	12.00	6.38	10.94
6.12	7.36	4.95	9.47	3.38	8.10
5.80	6.65	1.95	6.58	0.39	5.17

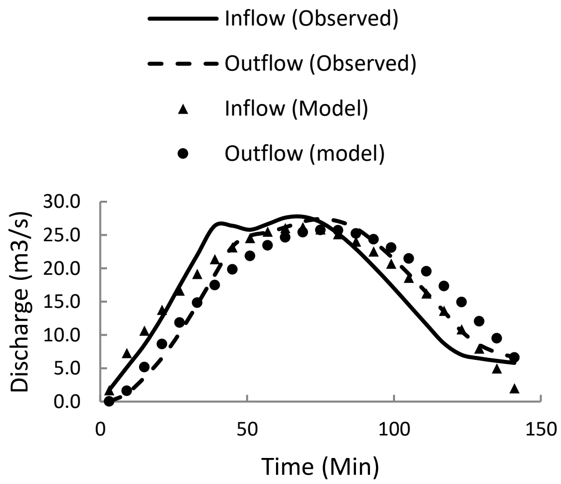

Figure 4. Observational inflow and outflow hydrograph of Chow et al. (1988)

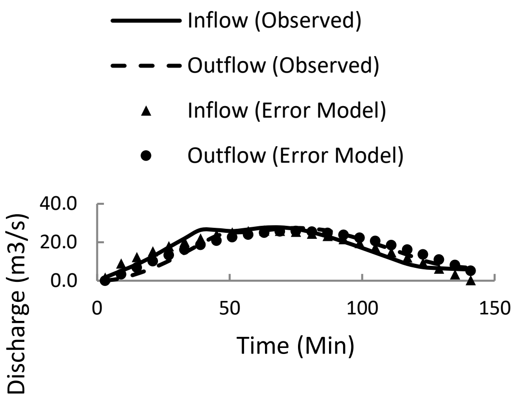

Figure 5. Flow model proposed by Choudhury and Sankarasubramanian (2009)

The reason for the difference in the data in Figure 4 and 5 are the use of different techniques in prediction. In this article, two methods includes the least squares error method, and neural networks have been used.

3. RESULTS

The networks utilized are Multi-Layer Perceptrons (MLP), which operate using a feed-forward back-propagation method. Research indicates that this type of network is effective for flood trend analysis and has been previously employed in related studies. Each network is structured with three layers: an input layer, an intermediate layer, and an output layer. The input layer consists of three neurons, while the output layer has one neuron that produces the output hydrograph. The performance function used is the Mean Squared Error (MSE), which evaluates the network's performance by calculating the average of the squared errors. The limitations on the number of layers and neurons in these networks are primarily due to the restricted amount of available data.

The performance of three trained networks is compared to the proposed model by Choudhury and Sankarasubramanian (2009). Figure 6 illustrates the effectiveness of the three transfer functions. Based on the mean absolute magnitude of the errors, we find that the tansig function has an error of 0.0359, the logsig function has an error of 0.0538, and the purelin function has an error of 0.0358. This indicates that both the tansig and purelin functions provide a better model. However, due to the superior prediction of peak discharge achieved by the tansig function, we accept it as the preferred model.

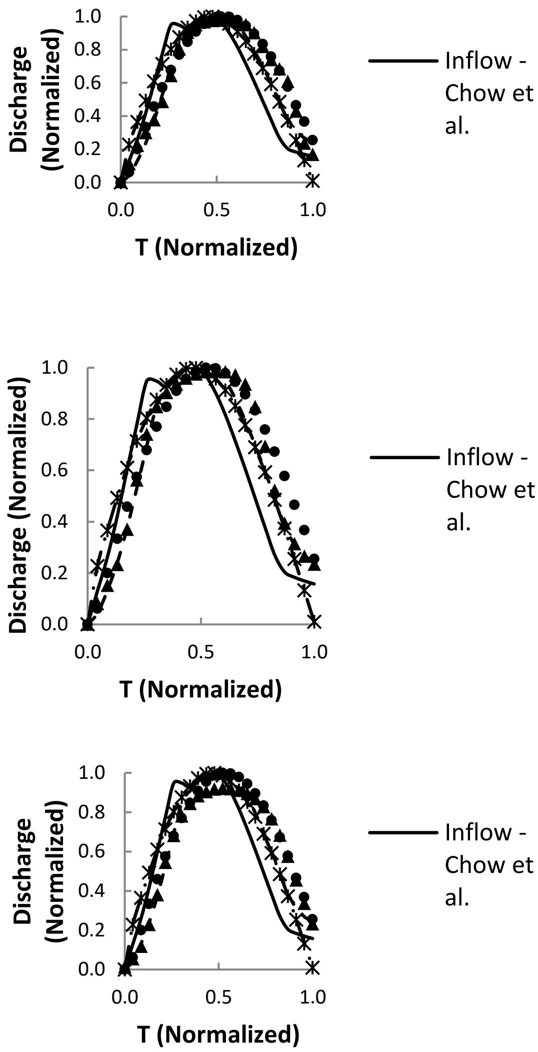

Figure 6. Comparison of the results of neural networks and the proposed model of Choudhury and Sankarasubramanian (2009) with different transfer functions including (a) tansig, (b)logsig, (c)purelin

In Figure 7, the proposed model is validated against the hydrograph developed by Choudhury and Sankarasubramanian (2009), referred to as the Error Model. The figure demonstrates that the proposed neural network model aligns well with the results of Choudhury and Sankarasubramanian's model.

Table 2 shows the mean absolute difference between the predictions of the neural network and the least squares method. From this data, we can conclude that while the neural network predictions are reasonably accurate, the least squares method has provided a relatively more precise value.

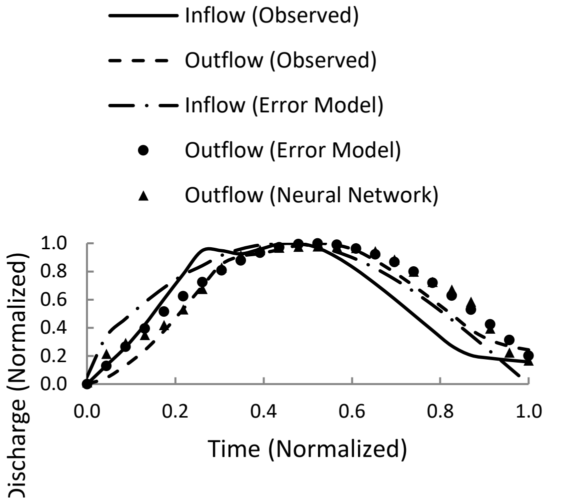

Figure 7. Comparison of results of neural networks and the proposed error model Choudhury and Sankarasubramanian (2009)

Figure 8 compares the results of the least squares method with those of the neural network.

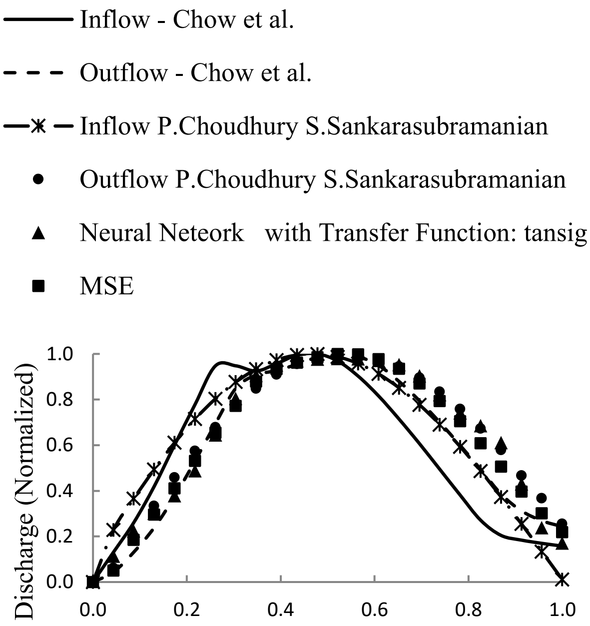

Figure 8. Comparison of results of neural networks, least squares error method, and the proposed model of Choudhury and Sankarasubramanian (2009)

Table 2 - Comparison of least squares error method and neural network

Method	neural networks	least squares error
RSME (%)	4.84	3.82

4. CONCLUSION

One of the most devastating disasters are Floods that can cause damage to ecosystems. Accurate simulation of floods are significantly important for flood control and the reduction of flood losses. There have been relatively limited studies in the field of reservoir routing using artificial intelligence models, and this is one of the innovations of the present article. This paper discusses flood routing using two methods: neural networks and the Muskingum method, which employs the least squares error approach. The models presented in this study are validated using the proposal by Choudhury and Sankarasubramanian (2009). Initially, the results of the neural network model using the transfer functions tansig, logsig, and purelin were examined. Ultimately, the proposed model was confirmed using the tansig function. The results were then compared to those obtained using the least squares error method. It was concluded that although both methods provide acceptable predictions, the least squares error method yields a relatively more accurate result.

References

[1] Agami, N., Atiya, A., Saleh, M., El-Shishiny, H. (2009). A neural network based dynamic forecasting model for Trend Impact Analysis. Technological Forecasting and Social Change, 76(7), 952-962.

[2] Al-Humoud, J. M., Esen, I. I. (2006). Approximate Methods For The Estimation Of Muskingum Flood Routing Parameters. Water Resources Management, 20(6), 979-990.

[3] Choudhury, P., Sankarasubramanian, A. (2009). River flood forecasting using complementary Muskingum rating equations. Journal of Hydrologic Engineering, 14(7), 745-751.

[4] Chow, V. T., Maidment, D. R., and Mays, L. W. (1988). Applied hydrology, International Ed., McGraw-Hill, New York.

[5] Chu, H.J., Chang, L.C. (2009). Applying particle swarm optimization to parameter estimation of the nonlinear Muskingum model. Journal of Hydrologic Engineering, 14(9), 1024-1027.

[6] Easa, S.M. (2013). Improved nonlinear Muskingum model with variable exponent parameter. Journal of Hydrologic Engineering, ASCE, 18(22), 1790-1794.

[7] Katipoğlu, O. M., Sarıgöl, M. (2023). Boosting flood routing prediction performance through a hybrid approach using empirical mode decomposition and neural networks: A case study of the Mera River in Ankara. Water Supply, 23(11), 4403-4415.

[8] Mirzazade, P. (2013). Investigation flood routing methods in river and reservoirs. M.Sc Thesis. Sistanand Baluchestan University. Civil college. Sistan and Baluchestan province. Iran. 86 (in Persian).

[9] Moghaddam, A., Behmanesh, J., Farsijani, A. (2016). Parameters estimation for the new four-parameter nonlinear Muskingum model using the particle swarm optimization. Water resources management, 30, 2143-2160.

[10] Mohan, S. (1997). Parameter estimation of nonlinear Muskingum models using genetic algorithm. Journal of hydraulic engineering, 123(2), 137-142.

[11] Niazkar, M., Afzali, S.H. (2014). Assessment of modified honey bee mating optimization for parameter estimation of nonlinear Muskingum models. Journal of Hydrologic Engineering, 20(4), p.04014055.

[12] Perumal, M. (1994). Hydrodynamic derivation of a variable parameter Muskingum method: 1. Theory and solution procedure. Hydrological sciences journal, 39(5), 431-442.

[13] Sarıgöl, M. (2024). Evaluating the Accuracy of Machine Learning, Deep Learning and Hybrid Algorithms for Flood Routing Calculations. Pure and Applied Geophysics, 181(12), 3485-3506

Scenario-Based Analysis of Reverse Flow and Hydraulic Backwater Effects on Dam Failures

Hasan Oğulcan MARANGOZ [*1] Tuğçe ANILAN [2]

[1] Recep Tayyip Erdoğan University, Faculty of Engineering, Department of Civil Engineering, Rize, Türkiye

[2] Karadeniz Technical University, Department of Civil Engineering, 61080 Trabzon, Türkiye

Received date**: 05.05.2025**; Accepted date**: 18.06.2025**; Published date: **28.06.2025**

Turkish Journal of Hydraulic, Vol : **9**, Number : **1**, Page, **33-41**, **(2025)**

e-ISSN: **2636-8382**

SLOI: http://www.dergipark.org.tr

*Correspondence: hasanogulcan.marangoz@erdogan.edu.tr

Abstract

In dam failure applications, the dam break mechanism and the outflow hydrograph are among the most uncertain factors. Therefore, 2D hydraulic modeling and analyzing dam failure scenarios, aiming to reduce uncertainties related to different failure mechanisms by creating 11 distinct scenarios, are carried out. During the modeling process, the interactions between the dam structure and the downstream flow area were evaluated through two-dimensional analyses, incorporating various failure types such as "overtopping" and "piping." According to the analysis results, peak flow rates varied between 6,510.06 m³/s and 33,004.04 m³/s depending on the scenario, while the time to reach peak flow ranged from 18 to 91 minutes. It aims to provide a negative backpressure of the hydraulic behavior of dam failures, contributing to risk management and emergency planning while offering critical insights to enhance safety factors in dam design.

Keywords: *Dam Break, Hydraulic Analysis, Risk Assessment, Reverse Flow, Outflow Hydrograph, Weir Flow*

1. INTRODUCTION

Dams play a vital role in modern water resource management, providing benefits such as flood control, hydroelectric power generation, irrigation, and domestic water supply (Bayazıt and Önöz, 2008). Despite their structural significance and engineered safety features, dam failures, though statistically rare, pose considerable risks to downstream communities, infrastructure, and the environment (MacDonald and Langridge-Monopolis, 1984; Abay and Baykan, 2015). The sudden release of large volumes of stored water can lead to catastrophic flooding, resulting in loss of life, economic damage, and long-term ecological disruption (Altinakar et al., 2011; Azeez et al., 2020; Wang et al.,2024).

Understanding the hydraulic behavior of dam breaches is essential for developing effective risk assessment tools and emergency response strategies (Bozkuş, 2004). The complexity of dam failure processes arises from the variety of potential failure mechanisms, including overtopping, internal erosion (piping), and structural instability (Broich, 1998; Basco, 1989). Each of these mechanisms generates distinct flood wave characteristics, making it necessary to evaluate a wide range of breach scenarios in hydraulic modeling studies (Bosa and Petti, 2013; Cao et al., 2011a; Pianforini et al., 2024).

Advancements in numerical modeling have enabled more accurate simulations of flood propagation following dam failures. Two-dimensional (2D) hydraulic models, in particular, allow for spatially distributed analysis of flow depth, velocity, and inundation extent, offering critical insights into how flood waves interact with natural topography and man-made structures (Cao et al., 2011b; Cao et al., 2020). Scenario-based modeling enhances this approach by accounting for uncertainties in breach development and enabling the exploration of worst-case outcomes under different assumptions (Bozkuş and Bağ, 2011).

In this study, a comprehensive scenario-based dam breach analysis was conducted using a 2D hydraulic modeling framework. A total of 11 distinct breach scenarios were developed to represent various failure types and conditions. The model incorporated detailed terrain and infrastructure data, including bridges, floodwalls, and urban features, to accurately simulate flow dynamics in the downstream floodplain.

Key hydraulic parameters such as peak discharge, flood wave arrival time, maximum water depth, and velocity distributions were evaluated across scenarios (Aydemir and Güven, 2017). The hydraulic roughness of natural channels and flood plains was also accounted for using established empirical values (Arcement and Schneider, 1989). The results support the creation of more resilient infrastructure and emergency planning procedures while also adding to a larger understanding of flood risks related to dam failures. This work supports continued initiatives to improve mathematical and physical modeling tools for disaster and dam failure simulations. (Brown and Rogers, 1981; Aris, 1990).

Some studies are intended to introduce new technologies on dam break prediction using advanced methods rather than a basic empirical approach, such as deep learning (Qiı et. al., 2024; Pianforini et. al., 2024; Deng et al., 2024; Al-Ghosoun et. al., 2024), remote sensing (Gouli et al., 2025) or specific model suggestion (Ma et al., 2024)

This study presents a scenario-based hydraulic analysis of dam failure using a two-dimensional (2D) numerical modeling approach. A total of 11 dam breach scenarios, representing different failure mechanisms such as overtopping and piping, were simulated to examine the spatial and temporal characteristics of resulting flood waves. Along the Galyan and Değirmendere streams, the model included comprehensive topographic and infrastructure data, such as bridges, floodwalls, and urban structures. Under each scenario, important hydraulic parameters were examined, including flow velocity, water depth, arrival time, and peak discharge. Notably, backwater and reverse flow effects were occasionally noted, particularly at confluence zones, and significantly impacted flood depth and velocity patterns. The results provide valuable insights for flood risk assessment, infrastructure design, and emergency planning in dam break events.

2. METHODOLOGY

Flood waves resulting from dam failures possess the destructive capacity to overwhelm virtually all structures located along the downstream path. The height of the resulting surge generally reaches its peak along the river on which the dam is situated. In such circumstances, the most critical concern involves bridges that enable pedestrian or vehicular passage across the river, which may be highly susceptible to overtopping or structural damage during a flood event.

Engineered structures located along the river are typically exposed to three categories of risk: partial submersion, complete submersion, or no impact at all if the flood waters remain below the base level of the structure. Therefore, these infrastructures were explicitly included in the simulation to capture their interaction with potential flood waves. Additionally, other flood-vulnerable structures such as floodwalls, retaining walls, and shoring systems were mapped onto the terrain model to ensure comprehensive risk assessment.

Downstream bridges, retaining walls, and flood protection systems were digitized using photogrammetric virtual mapping tools to facilitate accurate modeling. As shown in Figure 1, three central urban bridges labeled Bridges 1, 2, and 3 were mapped for their spatial dimensions using this virtual base. Cross-sectional data obtained along each bridge's axis provided vertical and longitudinal measurements, which are illustrated in Figure 2. The distances of these bridges from the dam along the assumed river centerline were measured as 18,342 m, 17,910 m, and 17,821 m, respectively.

These bridges were selected as representative urban structures due to their proximity to densely populated areas and their strategic importance in local transportation. Their interaction with the flood wave is critical, as structural overtopping or failure could significantly amplify downstream flood risks. Including such key infrastructure in the model According to the analysis, Bridge 1 has a height of 6 meters and a length of 89 meters, Bridge 2 stands approximately 7 meters tall with a 55-meter span, and Bridge 3 measures 6 meters in height and 83 meters in length. Each bridge includes sufficient under-clearance to allow the passage of water. A total of 18 bridges were defined and modeled similarly in the two-dimensional simulation environment, with detailed specification of their physical parameters.

Geometric data for the remaining downstream bridges are compiled in Tables 1 and 2, which present their distances along the central flow axis measured in meters from the dam toward the sea. For Bridges 16 and 17, which are not directly aligned with the centerline, the alignment is provided in terms of their perpendicular offset from this axis. These bridges are situated 88 meters apart over the Değirmendere Stream along the Yomra-Maçka road, measured from a defined origin point. The label"Distance-Elevation (1-2)" refers to the longitudinal profile of each bridge, where distance (in meters) is paired with corresponding elevation values. Each bridge was assigned two such measurement lines. Bridge width refers to the structure's transverse dimension in meters.

allows for a more realistic simulation of potential flood impacts and supports more informed emergency planning.

Figure 1. Digitized layout of Bridges

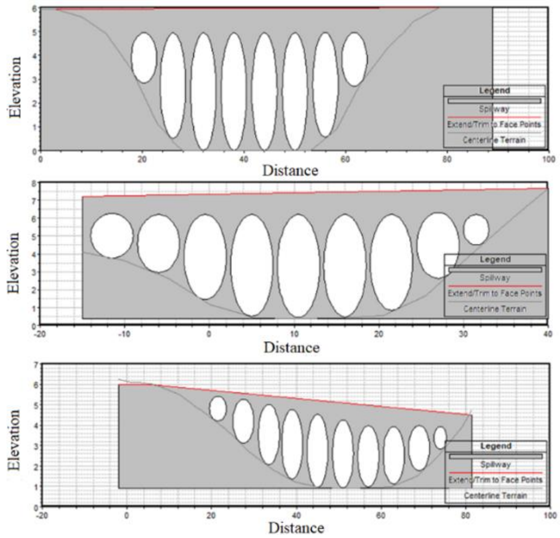

Figure 2. Elevation and longitudinal data for Bridges 1, 2, and 3

Table 1. Geometric properties of Bridges 12–19

Bridge Num.	**19**	**17**	**16**	**15**	**14**	**13**	**12**
Distance on RCR	531	5784	5813	7131	8820	9985	10979
Distance-Elevation (1)	0, 112	0, 111	0, 108	0, 95	0, 78	0, 70	0, 59
Distance-Elevation (2)	67, 111	32, 112	25, 107	63, 95	58, 77	48, 68	52, 60
Width	5	6	12	10	10	7	5

Table 2. Geometric properties of Bridges 4–11

Bridge Num.	**11**	**10**	**9**	**8**	**7**	**6**	**5**	**4**
Distance on RCR	11973	12075	13303	13579	14099	14747	16257	16905
Distance-Elevation (1)	0, 49	0, 48	0, 39	0, 34	0, 28	0, 25	0, 18	0, 11
Distance-Elevation (2)	44, 47	71, 46	36, 34	71, 34	46, 27	37, 25	82, 19	66, 10
Width	12	6	7	25	5	4	3	5

RCR: River Centerline Reference

The downstream floodwall, designated as Floodwall 8, was digitized in plan view, as shown in Figure 3.

Figure 3. Digitized layout of Floodwalls

Similar to the bridges, their length and width were defined in the plan view, while cross-sectional profiles provided elevation and distance data (Figure 4). The central alignment of this wall lies 11,883 meters from the dam along the river centerline. In total, eight protective structures comprising floodwalls, retaining walls, and shoring elements were modeled in this manner. Additional structural protections retaining walls, shoring systems, and flood barriers, were also analyzed for their top elevation and length. A plot of these values is presented in Figure 5. The alignments of Structures 1 through 6 along the river centerline are at distances of 17,250 m, 16,504 m, 15,102 m, 14,933 m, 14,537 m, 13,357 m, and 12,109 m, respectively.

Geometric data for buildings in the study area, including residential and commercial structures, were derived from a previous study (NFB, 2014) and integrated into the raster terrain model using ArcGIS-based elevation analysis. This integration is illustrated in Figures 6,7, and 8.

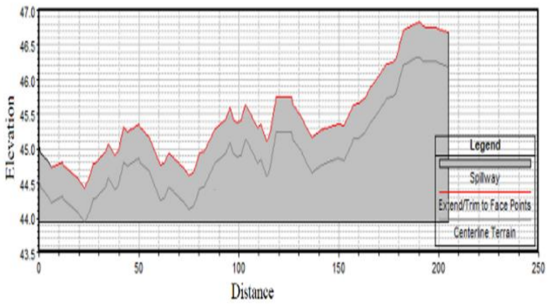

Figure 4. Elevation and distance profile of Floodwall 8

Photogrammetric data collection converts all surface features directly into elevation layers. As a result, certain elevated structures, such as bridges may be erroneously embedded into the terrain model. This misrepresentation is visible in Figure 7, where bridges are incorporated as continuous ground elements. Such features were removed from the raw elevation map and redefined based on their actual geometry to ensure accurate modeling (Figure 8).

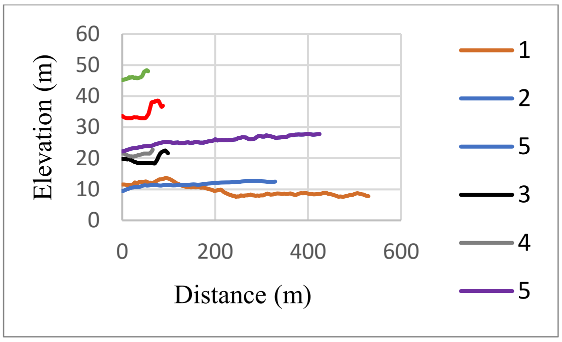

Figure 5. Variation in crest elevation of floodwalls along the river centerline

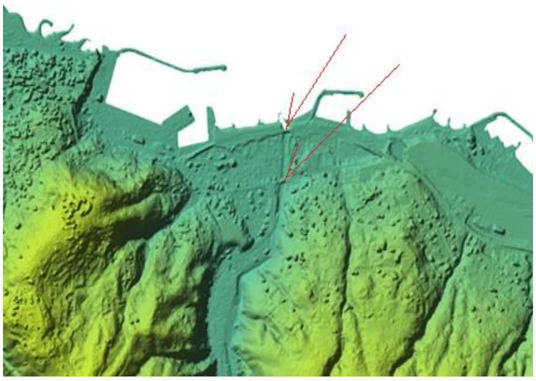

Figure 6. Raw terrain model of the urban center

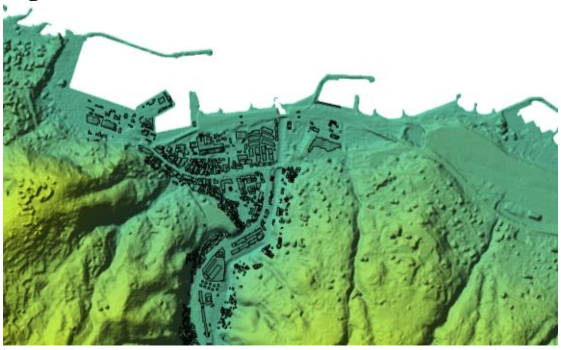

Figure 7. Digitized buildings mapped over an elevation base

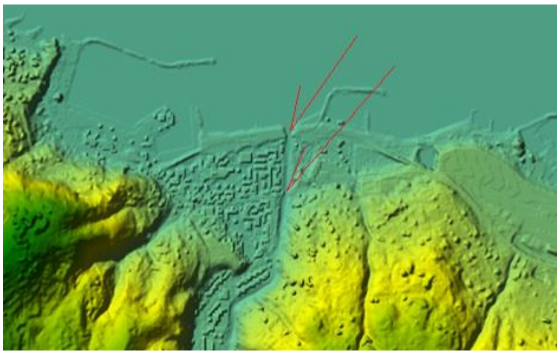

2.1. Hydraulic Parameters

The two-dimensional hydraulic model employed in this study relies on a set of physical assumptions to define downstream water behavior.

Among these are the assumptions that the flood wave behaves as an incompressible, homogeneous fluid and that temperature variations throughout the domain are negligible. The dam failure and flood propagation processes were modeled separately to provide clearer insight into each phenomenon.

The reservoir was assumed to contain clean, sediment-free water, and the downstream riverbed was treated as a dry floodplain at the onset of simulation. The entire study area was discretized into a two-dimensional computational mesh to represent flow dynamics.

2.1.1 .Definition of Breach Parameters

The dynamics of dam failure inherently involve significant uncertainty. Multiple breach parameters were developed and tested to explore a range of potential failure mechanisms to address them. A total of eleven dam breach scenarios were constructed (Table 3), allowing for a comprehensive assessment of possible outcomes and the reduction of modeling uncertainty.

In the breach simulations, the dam structure acts as a boundary interface between the upstream reservoir and the downstream mesh-defined flow domain. The maximum dam height used in the model, measured at the crest including the parapet wall, was 320.55 meters. This elevation was taken as the catastrophic water level, representing the upper bound of reservoir capacity.

In the flood propagation model, downstream mesh elements ranged in size from 177.51 m² to 450.67 m², with an average cell area of approximately 225 m², based on a 15×15 m grid resolution. The total number of computational cells in the downstream domain reached up to 6,967.

Flow through the breach was modeled as a broad-crested weir, with a discharge coefficient (Cd) set at 1.66. A linear relationship was assumed between time and the breach enlargement process to simplify the breach evolution (Table 3)

Figure 8. Integration of building data and correction of elevation anomalies in the riverbed

Table 3. Summary of Dam Breach Scenarios Used in the Model

Scenario	Final breach base elevation (m)	Final breach base width (m)	Horizontal coordinate of the breach base center (m)	The right and left slopes of the breach	Break Time, t_f (saat)	Breach Model	Res. Water Elevation (m)	Break Type
1	240	20	200	2	0.4	-	316.5	OT
2	240	20	200	2	0.67	-	316.5	OT
3	240	20	200	2	0.67	-	319.05	OT
4	240	13	200	0.5	1.98	MacDonald et al.	319.05	OT
5	240	31	200	1	0.43	Froehlich (2008)	319.05	OT
6	240	29	200	0.7	0.43	Froehlich (2008)	319.05	PE
7*	240	29	200	0.7	0.43	Froehlich (2008)	319.05	PE
8	240	43	200	2	0.4	-	320.55	OT
9	240	43	200	1.4	0.52	Froehlich (1995)	320.55	OT
10	240	216	200	0.5	1.86	Von Thun & Gillette (1990)	320.55	OT
11	240	113	200	1.03	1.34	Xu & Zhang (2009)	320.55	OT

FM: Full Momentum Solution, OT: Overtopping, PE: Piping Erosion

2.1.2 .Selection of Time Step

Under unsteady flow conditions, every parameter of the dam-break flood wave varies continuously over time. Therefore, the computational time step (dt) must be sufficiently small to accurately resolve these variations. The dt itself needs to be fine enough to record dynamic changes at every stage of the flow path, even though it lacks a fixed real-world analog.

The time step in shallow water simulations is equivalent to the model's numerical resolution interval. One second was chosen as the time step for this investigation. Additionally, output data was recorded at 1-minute intervals. In risk maps and flood hydrograph analyses, ensuring both temporal accuracy and clarity in result interpretation.

2.1.3. Boundary Condition

Boundary conditions were used to incorporate model elements that do not exist physically but are necessary for simulation. These were applied both upstream and downstream to control inflow and outflow behavior (Figure 9).

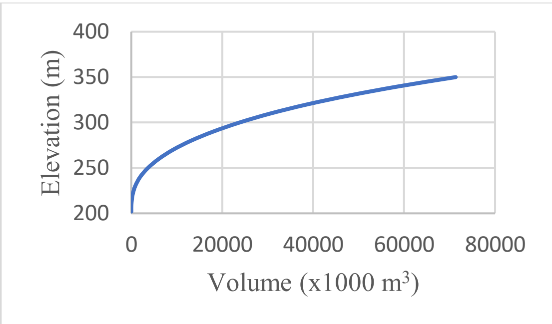

Figure 9. Elevation–Volume Curve Defined for the Reservoir

In the breach model, the upstream boundary was defined by the dam reservoir, while the downstream boundary consisted of a normally distributed flood wave depth. The elevation–volume curve used for the reservoir was derived from the study by NFB (2014) and is shown in Figure 9.

The reservoir was characterized by a normal water level of 316.50 m, a maximum level of 319.05 m, and a catastrophic water level of 320.55 m. Breach simulations were conducted under these static reservoir conditions, and the resulting outflow hydrographs representing the dam failure discharge were recorded for use in subsequent propagation modeling.

Downstream, the riverbed was initially assumed to be dry, with a single outlet defined at the downstream boundary. The flood wave reaching this point was assumed to follow the terrain slope as it continued beyond the model domain. The bed slope at the outlet was set at 0.02.

In the flood propagation model, all boundary conditions were located downstream of the dam. The dam breach hydrograph obtained from the failure model was applied as the upstream input for this stage. The terminal boundary was set at the land-sea interface, where a single outlet was defined with a slope value of 0.012, assuming the continuation of the terrain gradient. The influence of sea level or tidal effects was not incorporated in this model .

The simulation results revealed that maximum flood depths reached up to 43 meters in the main channel of the Galyan Stream and 37 meters in its adjacent floodplain. At the confluence with the Değirmendere Stream, peak water depths approached 24 meters. A negative wave effect, typically associated with diffusive wave propagation, was also observed using the dynamic wave model at the junction of Galyan and Değirmendere. This reverse wave movement extended approximately 1,830 meters upstream from the confluence point (Figure 10). During this reverse flow period, the peak water elevation reached 22.7 meters in the main channel and 18.6 meters in the floodplain.

Analysis of the average flow patterns indicates that water depths increased steadily over the first 600 meters, following initial dam breach discharge. Beyond this, the flood wave showed abrupt fluctuations before decreasing steadily up to 8,116 meters. As the flood progressed along Değirmendere, the water depth began to increase again, reaching its maximum at 11,968 meters, where the peak depth was recorded as 35.3 meters, the highest value observed along the entire downstream path of the Değirmendere Stream. In contrast, the maximum flood depth within the urban section of the main river channel was measured at 18.03 meters, recorded at the 16,256-meter mark along the river centerline. This value declined irregularly beyond that point as the flow continued through the city.

Figure 10. Negative wave reflection at the confluence of Galyan and Değirmendere Streams

Flow velocities measured downstream of the dam along the river centerline are calculated separately. These values represent the flood behavior at the 49th minute (Figure 11), the moment when the flood wave first reaches the sea boundary. The highest flow velocity observed along the Galyan Stream was 9.8 m/s, while the confluence with the Değirmendere Stream registered a lower velocity of 1.53 m/s. The overall maximum velocity, however, was recorded further downstream at 12,500 meters, where it peaked at 13.25 m/s. In general, velocity distributions exhibited rapid and irregular fluctuations along the main channel, a pattern that persisted through the urban center. The highest velocity within the city was recorded at 10.86 m/s, and the mean flow velocity in this region was calculated as 5.43 m/s.

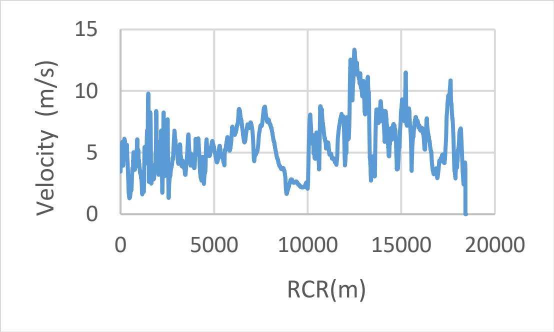

Figure 11. Flow velocity distribution at 49 minutes along the river centerline

3. CONCLUSION

This study presented a comprehensive scenario-based analysis of dam failure mechanisms using a two-dimensional hydraulic modeling approach by simulating 11 different failure scenarios, ranging from overtopping to piping erosion.

Simulation results demonstrated that peak flow discharges varied widely, from 6,510.06 m³/s to 33,004.04 m³/s, with the time to peak ranging between 18 and 91 minutes, depending on the scenario. These variations highlight the necessity of scenario diversity in capturing the full spectrum of flood behavior.

Hydraulic impacts were most severe along the Galyan and Değirmendere streams. The maximum flood depth reached 43 meters in the main river channel and 37 meters in adjacent floodplains. At the confluence with the Değirmendere Stream, water levels peaked at 24 meters, while a reverse wave propagated upstream for approximately 1,830 meters, producing local maximum depths of 22.7 meters in the main channel and 18.6 meters in the floodplain.

The analysis also revealed highly variable velocity distributions. Peak flow velocities reached 13.25 m/s at 12,500 meters downstream, while urban sections of the river experienced velocities up to 10.86 m/s, with an average of 5.43 m/s. These values underscore the risk posed to critical infrastructure, particularly in urban zones with high population density and vulnerable structures such as bridges and floodwalls.

Overall, the scenario-based framework adopted in this study offers a novel methodology for evaluating dam breach impacts. It provides essential input for emergency response planning, structural design enhancements, and the development of risk-informed flood mitigation strategies. Future studies could benefit by integrating sediment transport and real-time data assimilation to refine predictive capabilities in river analysis systems further.

REFERENCES

[1] Abay, O., Baykan, N., (2015). Reasons for dam failures throughout history. Proceedings of the 4th Water Structures Symposium, 19–21 November, Ankara, pp. 157–166.

[2] Altinakar, M.S., Riffai, M.A., Bergman, N., Bradford, S.F., (2011). Earthen embankment breaching. Journal of Hydraulic Engineering, 137(12), 1549–1564.

[3] Arcement, G.J., Schneider, V.R., (1989). Manning's roughness coefficients for natural channels and floodplains. U.S. Geological Survey Water-Supply Paper, 2339.

[4] Aris, R., (1990). Vectors, Tensors, and the Basic Equations of Fluid Mechanics. Dover Publications, ISBN: 0486661105, 320 p.

[5] Aydemir, A., Güven, A., (2017). Comparison of discharge estimation methods used in dam break models. HU Journal of Engineering, 1, 22–29.

[6] Azeez, O., Elfeki, A., Kamis, A.S., Chaabani, A., (2020). Dam break analysis and flood disaster simulation in arid urban environment: the Um Al-Khair Dam case study, Jeddah, Saudi Arabia. Natural Hazards, 100, 995–1011.

[7] Basco, D.R., (1989). Limitations of de Saint Venant equations in dam break analysis. Journal of Hydraulic Engineering, 115(7), 950–965.

[8] Bayazıt, M., Önöz, B., (2008). Flood and Drought Hydrology. Nobel Academic Publishing, 1st Edition, ISBN: 6053951421, 259 p. [In Turkish]

[9] Bosa, S., Petti, M., (2013). A numerical model of the wave that overtopped the Vajont Dam in 1963. Water Resources Management, 27, 1763–1779.

[10] Bozkuş, Z., Bağ, Z., (2011). Virtual failure analysis of Çınarcık Dam. IMO Technical Journal, 364, 5675–5688. [In Turkish]

[11] Bozkuş, Z., (2004). Dam break analysis for disaster management. IMO Technical Journal, 224, 3335–3350. [In Turkish]

[12] Broich, K., (1998). Mathematical modelling of dam-break erosion caused by overtopping. Concerted Action on Dam Break Modelling, 2nd Project Workshop, Munich, Germany.

[13] Brown, R.J., Rogers, D.C., (1981). BRDAM Users' Manual. Water and Power Resources Service, Denver, 67 p.

[14] Cao, Z., Yue, Z., Pender, G., (2011a). Landslide dam failure and flood hydraulics. Part I: Experimental investigation. Natural Hazards, 59(2), 1003–1019.

[15] Cao, Z., Yue, Z., Pender, G., (2011b). Landslide dam failure and flood hydraulics. Part II: Coupled mathematical modelling. Natural Hazards, 59(2), 1019–1045.

[16] Cao, J.G., Feal, O.G., Nóvoa, D.F., Gesteira, M.G., (2020). Iber+: A new code to analyze dam-break floods. Proceedings of the 2nd International Workshop on Natural Hazards, 23–26 June, Pico Island.

[17] NFB Engineering (2014). Flood Analysis of Atasu Dam-Break, Technical Report, Ankara, Türkiye, 544 s.

[18] MacDonald, T.C., Langridge-Monopolis, J., (1984). Breaching characteristics of dam failures. ASCE Journal Hydraulic Engineering, 110(5), 567-586.

[19] Froehlich, D. C., (1995), Peak outflow from breached embankment dam. Journal of Water Resources Planning and Management, 121(1), 90-97.

[20] Singh, K.P. Snorrason, A., (1984) Sensitivity of outflow peaks and flood stages to the selection of dam breach parameters and simulation models. Journal of Hydrology. 68, 295-310.

[21] Froehlich, D.C., (2008). Embankment Dam Breach Parameters and Their Uncertainties. Journal of Hydraulic Engineering. 134(12), 1708-1721.

[22] Von Thun, J.L., Gillette, D. R., (1990). Guidance on Breach Parameters, Internal Memorandum. Unpublished Internal Document.

[23] Qiu, W., Li, Y., Zhang, Y., Wen, L., Wang, T., Wang, J., & Sun, X. (2024). Numerical investigation on the evolution process of cascade dam-break flood in the downstream earth-rock dam reservoir area based on coupled CFD-DEM. Journal of Hydrology, 635, 131162.

[24] Pianforini, M., Dazzi, S., Pilzer, A., & Vacondio, R. (2024). Real-time flood maps forecasting for dam-break scenarios with a transformer-based deep learning model. Journal of Hydrology, 635, 131169.

[25] Ma, B., Zhou, J., & Zhang, C. (2024). Risk Prediction Model for Tailings Ponds Based on EEMD-DA-LSTM Model. Applied Sciences, 14(19), 9141.

[26] Deng, Y., Zhang, D., Cao, Z., & Liu, Y. (2024). Spatio-temporal water height prediction for dam break flows using deep learning. Ocean Engineering, 302, 117567.

[27] Al-Ghosoun, A., Gumus, V., Seaid, M., & Simsek, O. (2025). Predicting morphodynamics in dam-break flows using combined machine learning and numerical modelling. Modeling Earth Systems and Environment, 11(1), 74.

[28] Gouli, M. R., Hu, K., Khadka, N., Liu, S., Yifan, S., Adhikari, M., & Talchabhadel, R. (2025). Quantitative assessment of the GLOF risk along China-Nepal transboundary basins by integrating remote sensing, machine learning, and hydrodynamic model. International Journal of Disaster Risk Reduction, 105231.

[29] Xu, Y., & Zhang, L. M. (2009). Breaching parameters for earth and rockfill dams. Journal of Geotechnical and

Geoenvironmental Engineering, 135(12), 1957-1970.

On the Effect of Hysteretic Behavior on the Residual Energy and Flow Regime in the Sudden and Gradual Contraction

Ehsan Aminvash[*1] **Maryam Menazadeh**[2]

[1] Department of Civil Engineering, University of Tabriz, Tabriz, Iran.

[2] Recep Tayyip Erdoğan University, Faculty of Engineering, Department of Civil Engineering, Rize, Türkiye.

Received date**: 29.05.2025**; Accepted date**: 16.06.2025**; Published date: **28.06.2025**

Turkish Journal of Hydraulic, Vol : **9**, Number : **1**, Page , **42-54**, **(2025)**

e-ISSN: **2636-8382**

SLOI: http://www.dergipark.org.tr

*Corresponding author e-mail: E.aminvash@tabrizu.ac.ir

Abstract

In the present study, the hysteretic behavior of supercritical flow that can occur in a canal near adjacent structures, including cross-sectional contractions of the canal width, has been investigated experimentally. Three sudden contracting of 5, 10 and 15 cm and a gradual contraction of 15 cm have been used. The flow rates ranged from 250 to 600 Lit/min. These conditions are set within a laboratory flume; first there is an increase in the initial flow and then a decrease in secondary flow. The results show that by increasing and then decreasing the flowrate, two different behaviors of flow are observed with the same laboratory conditions. The results showed that with increasing the rate of sudden contracting, the values of relative depths decrease, so that in the initial flow these depths indicate a subcritical regime and in the secondary flow with the formation of hysteresis in some discharges indicate a supercritical regime. Also, hysteretic behavior increases the relative residual energy. With the sudden contraction of 15 cm, the formation of submerged hydraulic jumps resulted in a lack of hysteresis.

Keywords: Hysteresis; Flow regimes; Sudden and gradual contraction; Relative residual energy; Relative depth.

1. INTRODUCTION

The main purpose of this study was to investigate the contradictory behavior of supercritical flow in dealing with the sudden and gradual contraction in which both conditions of formation and non-formation of hydraulic jump are possible. The existence of such contradictory behavior occurs due to the phenomenon of hysteresis, for which there are relatively limited studies to identify it. Generally, the occurrence of the hysteresis phenomenon in the collision of the flow with the obstacle is expected. As for the same input flow, two different behaviors are observed that this different behavior depends on the flow history.

The first category of studies on the phenomenon of hysteresis, which examines the bed hump of the canal, goes back to the research of Abbecasis and Quintela [1].

In the following, relatively extensive studies of the behavior of hydraulic hysteresis have been studied theoretically and experimentally on bed humps with a fixed width. For example, the following studies can be mentioned: Baines and Davies; Austria Lawrence and Austria investigated the hysteretic behavior of the flow on the bed hump of the canal by catastrophe theory [2-4].

The results showed that catastrophe theory can be used as a descriptive model that this method is based on the use of classical flow equations such as specific energy equations along with catastrophe theory.

Lawerence studied the steady flow through the bed hump and its various behaviors [4]. The results showed that there may be two stable states for the same input conditions that lead to the formation of the hysteresis loop (The mean of the hysteresis loop is to increase the discharge to a certain value and then gradually decrease it to the initial discharge and the formation of the hysteresis phenomenon in this interval, which occurs is a cycle). Baines and

Whitehead investigated the hysteretic behavior of the flow on the bed hump theoretically and experimentally. Theoretical and experimental results showed that under the same conditions of the input flow, two different states are created for the stability of the flow, which indicates the existence of a hysterical loop [5].

Defina and Susin first theoretically provided equations to study this phenomenon on the bed hump and then examined it experimentally [6].

They defined two weak and strong interactions at the same input flow conditions for the flow, which is a weak interaction (WI) when the flow regime is supercritical and does not affect the change of the flow regime. In contrast, a strong interaction (SI) indicates a condition in which the flow regime to subcritical due to a hydraulic jump.

The second category of studies that deals with contraction of the flow path can be referred to the research of Akers and Bokhove [7].

They theoretically and fieldally studied hysteretic behavior in gradual contraction. The results showed that the diagonal waves of the supercritical flow can be affected by other effects such as surface tension. Defina and Viero examined different states of flow created by gradual constriction [8].

The results of numerical and experimental studies showed that the friction and slope of the canal bed affect the flow stability and can create different hysteretic loops. Using classical hydraulic equations and catastrophic theory, Sadeghfam et al. investigated the hysteretic behavior of a supercritical flow in the face of localized canal narrowing [9].

Their experimental results showed that the application of relations related to catastrophic theory along with classical equations can describe hysteretic behavior. Daneshfaraz et al. experimental investigation of the effect of different sill geometry on hysteretic behavior of supercritical regime [10].

Viero and Defina investigated multiple states created by supercritical flow near a sluice gate. Investigations have been performed based on the upstream and downstream Froude number of the gate and the opening ratio of the valve by presenting a theory to predict the occurrence of hysteresis in the vicinity of the sluice gate. The results showed that for a certain amount of gate opening, two different behaviors of flow are observed, in one case the flow has a subcritical regime and in the other case it has a supercritical regime. The experiments also showed the validity of the theory presented to examine the up and downstream Froude numbers [11].

Daneshfaraz et al. conducted to laboratory and theoretical study of hysteretic effects on hydraulic characteristics of flow at the site of smooth to rough bed conversion [12-13].

The results show that by first increasing the flow rate and then decreasing it, different flow behaviors are observed for the same laboratory conditions: with increasing flow, the relative depth indicates that the flow is in the subcritical regime, whereas decreasing the flow demonstrates supercritical behavior. Also, Daneshfaraz et al. conducted to experimental study of hysteretic behavior of supercritical regime on hydraulic parameters of flow against gabion contraction [14].

Results showed that with the formation of the phenomenon of hysteresis, the relative depths of the flow were increased by 69.39% and the Froude number of the gabion contraction section has increased significantly by 69.15% and the main cause of the hysteretic behavior of the flow is the current behavior of the flow following its previous behavior. Recently, multiple steady flow states in spindle shaped geometry of bridge foundations conducted by Daneshfaraz et al. [15].

A review of previous research shows that despite theoretical and experimental studies of hysteretic behavior of flow; more extensive studies are needed to investigate the unknown dimensions of flow behavior.

These unknown dimensions are more noticeable in obstacles such as bridge piers, which have been more or less mentioned in previous studies, but little research has been done on the contracting of the flow path and the relative depths of the flow on the effect of hysteretic behavior on residual relative energy and longitudinal profiles have not been studied so far. In general, theoretical equations in such obstacles are less consistent with experimental results than in other obstacles. This may be due to the fact that the flow pattern against these obstacles does not allow the development of an accurate theory consistent with the one-dimensional flow approach. Therefore, in the present study, for the first time, the effect of hysteresis phenomenon on the relative residual energy, relative depths of the flow and longitudinal profiles of the flow in sudden and gradual contracting have been investigated.

2. METHODOLOGY

2.1. Experimental Set-Up

A laboratory flume with dimensions 5m in length, 0.5 m in height, and 0.3m in width was used in the experiments.

There was no slope and the walls and floor were made transparent. To create a supercritical flow, a vertical metal gate with an opening of 2 cm, located at a distance of 1.5 meters from the inlet tank, was used.

The inlet flow to the flume is provided by two pumps, each with a capacity of 450 liters per minute. Flow rate was measured using rotameters installed on the pumps.

In order to measure the flow depth, a point depth gauge with an error of ±1 mm was used, and glass boxes were deployed to create a contraction in the flow.

The present study is examined with four models, three of which are sudden contractions and one of which is gradual contraction.

Detailed information on the cases is presented in Table 1. Figure (1) shows the hydraulic jump profiles formed by the placement of the constriction elements in the flow path and the location of the flow depth measurements.

Table 1. Values of parameters in experiments

Case Study (CS) no.	Q (Lit/min)	b (sum of the two sides, cm)	Δb=B-b (cm)	Reynolds value	y_c (cm)	y_1 (cm)	y_2 (cm)
CS 1	250~600	5.0	25.0	50000~112000	2.7~5.28	1.52~5.07	2.08~4.82
CS 2		10.0	20.0			1.38~7.00	2.33~4.25
CS 3		15.0	15.0			5.23~9.98	3.12~5.46
CS 4		Gradual	Gradual			1.72~8.23	2.60~8.70

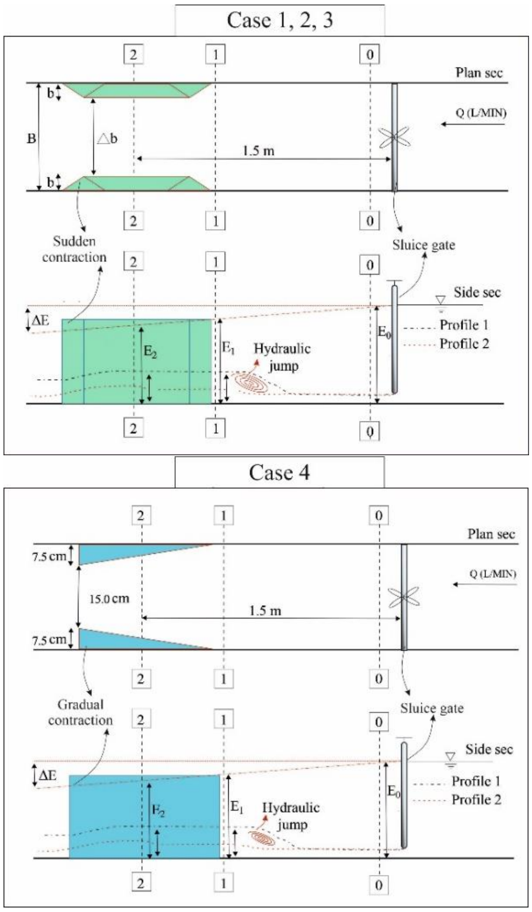

Figure 1. Profile in hydraulic jump and measured sections for sudden and gradual contractions

2.2. Dimensional Analysis

The parameters that govern hydraulic hysteretic behavior are listed in Eq. 1.

$$f1(Q,\rho,g,a,B,\Delta b,y_0,y_1,y_2,E_0,\\ E_1,E_2,x,V_0,V_1,V_2)=0 \tag{1}$$

Here, Q is discharge, ρ is density, g is gravity, a is the gate opening, B is the canal width, Δb is the shortened canal width, y_0 refers to the *vena contract* depth, y_1 is flow depth in section 1, y_2 is flow depth in section 2, E_0 represents the flow energy at the *vena contract*, E_1 and E_2 are the energy in sections 1 and 2, respectively. The symbol x is distance from the center of contraction to the gate, V_0, V_1, and V_2 are velocities in sections 0, 1, and 2, respectively. The dimensional analysis considered parameters g, ρ and y_0 as iterative parameters, the non-dimensional parameters are presented as Eq. 2.

$$f2(Fr_0,Fr_1,Fr_2,\mathrm{Re}_0,\frac{a}{y_0},\frac{B}{y_0},\frac{\Delta b}{y_0},\frac{y_1}{y_0},\\ \frac{y_2}{y_0},\frac{E_0}{y_0},\frac{E_1}{y_0},\frac{E_2}{y_0},\frac{x}{y_0})=0 \tag{2}$$

Further simplification of the parameters results in:

$$f3(Fr_0,Fr_1,Fr_2,\mathrm{Re}_0,\frac{a}{y_0},\frac{\Delta b}{B},\frac{y_1}{y_0},\\ \frac{y_2}{y_0},\frac{y_1}{y_2},\frac{E_1}{E_0},\frac{E_2}{E_0},\frac{x}{y_0})=0 \tag{3}$$

The flows in the present study are fully turbulent and the Reynolds number effect can be neglected [16-18].

Also, parameters a/y_0 (rate of gate opening), x/y_0 (distance between valve and the contracting). The final functional relationship is:

$$\frac{E_1}{E_0},\frac{E_2}{E_0},\frac{y_1}{y_0},\frac{y_1}{y_2},\\ \frac{y_2}{y_0},Fr_1,Fr_2=f4(Fr_0,\frac{\Delta b}{B}) \tag{4}$$

3. RESULTS and DISCUSSION

3.1. Longitudinal profiles

Longitudinal profiles of a supercritical flow collide with sudden and gradual constrictions that are shown in Figures 2 to 4. As mentioned, the flow rates of 250 to 600 liters per minute increased incrementally and subsequently decreased incrementally. With increasing and decreasing flow rates, two different behaviors of the flow are seen in several identical flows, providing evidence of hysteretic behavior. Tables 2 and Figs. 2-4 summarize the experiments performed and present the hysteretic behavior of the flow. The constriction elements located in the flow path cause a hydraulic jump and sections 1 and 2 are both subcritical. As the flow rate increases, the hydraulic jump moves downstream, and the flow regime becomes supercritical along the entire length of the canal. As the flow rate decreases, there are occurrences of different flow behaviors in the canal with sections 1 and 2 having supercritical flow.

Table 2. Hydraulic parameters for all case studies

Figure	Fr_0 (*vena contracta*)	Regimes		Profile	Flow history	CS no.
		Section 1	Section 2			
4a	2.339	Subcritical	Subcritical	P1	Flow increasing	CS1
4b	3.248	Subcritical	Subcritical	P1	Flow increasing	CS1
4c	4.149	Supercritical	Supercritical	P2	Increased flow caused supercritical hysteresis	CS1
4d	5.281	Supercritical	Supercritical	P2	Flow increasing	CS1
4e	4.149	Supercritical	Supercritical	P2	Decreasing flow	CS1
4f	**3.248**	**Supercritical**	**Supercritical**	**P2**	**Decreasing flow**	**CS1**
4g	**2.339**	**Supercritical**	**Supercritical**	**P2**	**Decreasing flow**	**CS1**
4h	1.666	Subcritical	Subcritical	P1	Decreasing flow caused subcritical hysteresis	CS1
5a	2.339	Subcritical	Subcritical	P1	Flow increasing	CS2
5b	3.248	Subcritical	Subcritical	P1	Flow increasing	CS2
5c	4.149	Subcritical	Subcritical	P1	Flow increasing	CS2
5d	5.263	Supercritical	Supercritical	P2	Increased flow caused supercritical hysteresis	CS2
5e	**4.149**	**Supercritical**	**Supercritical**	**P2**	**Decreasing flow**	**CS2**
5f	**3.248**	**Supercritical**	**Supercritical**	**P2**	**Decreasing flow**	**CS2**
5g	2.339	Subcritical	Subcritical	P1	Decreasing flow caused subcritical hysteresis	CS2
6a	2.339	Subcritical	Subcritical	P1	Flow increasing	CS4
6b	3.248	Subcritical	Subcritical	P1	Flow increasing	CS4
6c	4.149	Subcritical	Subcritical	P1	Flow increasing	CS4
6d	5.263	Supercritical	Supercritical	P2	Increased flow caused supercritical hysteresis	CS4
6e	**4.149**	**Supercritical**	**Supercritical**	**P2**	**Decreasing flow**	**CS4**
6f	**3.248**	**Supercritical**	**Supercritical**	**P2**	**Decreasing flow**	**CS4**
6g	2.339	Subcritical	Subcritical	P1	Decreasing flow caused subcritical hysteresis	CS4

Figure 2 shows the regime changes and the longitudinal profiles of the flow in the face of a sudden 5 cm contraction. By increasing the flow rate to 350 liters per minute (Figures 2a and 2b), sections 1 and 2 experience subcritical flow. When the flow rate reaches 400 liters per minute, the flow regime changes to supercritical. Then, with a gradual decrease in flow rate up to 350 liters per minute (Figures 2e and 2f), sections 1 and 2 are still supercritical until the flow rate reaches 300 liters per minute where sections 1 and 2 are subcritical.

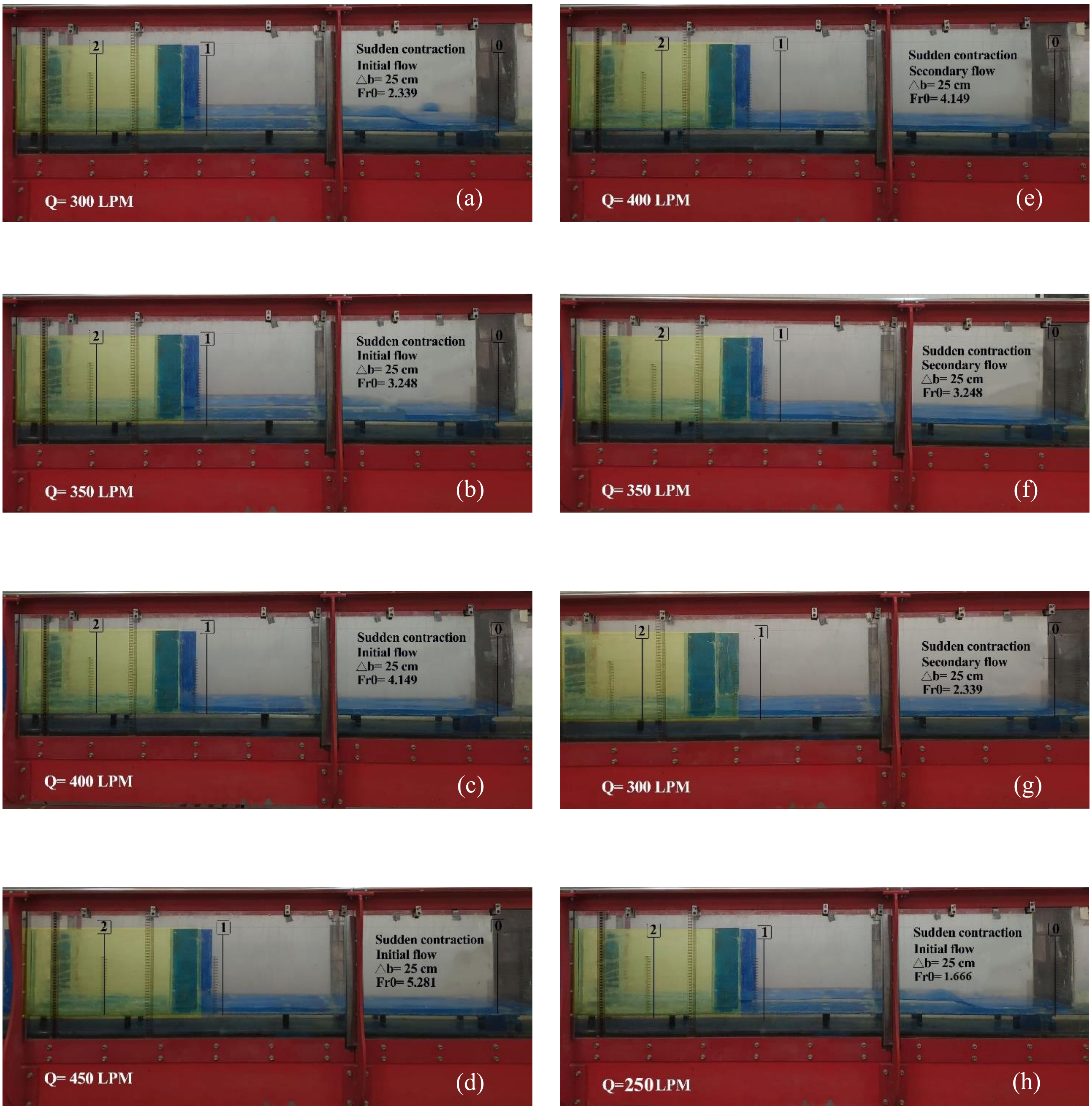

Figure 2. CS1 Experimental test runs

Figure 3 shows flow regimes and the longitudinal profiles of the flow for a sudden narrowing of 10 cm. With increasing flow up to 400 liters per minute (Figure 3a to 3c), sections 1 and 2 are subscribed. When the flow rate reaches 450 liters per minute, the flow regime changes at times to supercritical.

Then, with a gradual decrease in flow rate to 350 liters per minute (Figure 3e and 3f), sections 1 and 2 are still supercritical until a flow rate of 300 liters per minute is reached and sections 1 and 2 are subcritical.

Figure 3. CS2 Experimental test runs

Figure 4 shows regime changes and longitudinal profiles of the flow in the face of a gradual contraction. With increasing flow up to 450 liters per minute (Figures 4a-4c) sections 1 and 2 are subcritical. When the flow rate reaches 500 liters per minute, the flow regime changes intermittently to the supercritical regime. Then, with a gradual decrease in flow rate to 400 liters per minute (Figure 5e and 5f), sections 1 and 2 are still supercritical until a flow rate of 350 liters per minute is achieved and sections 1 and 2 are subcritical.

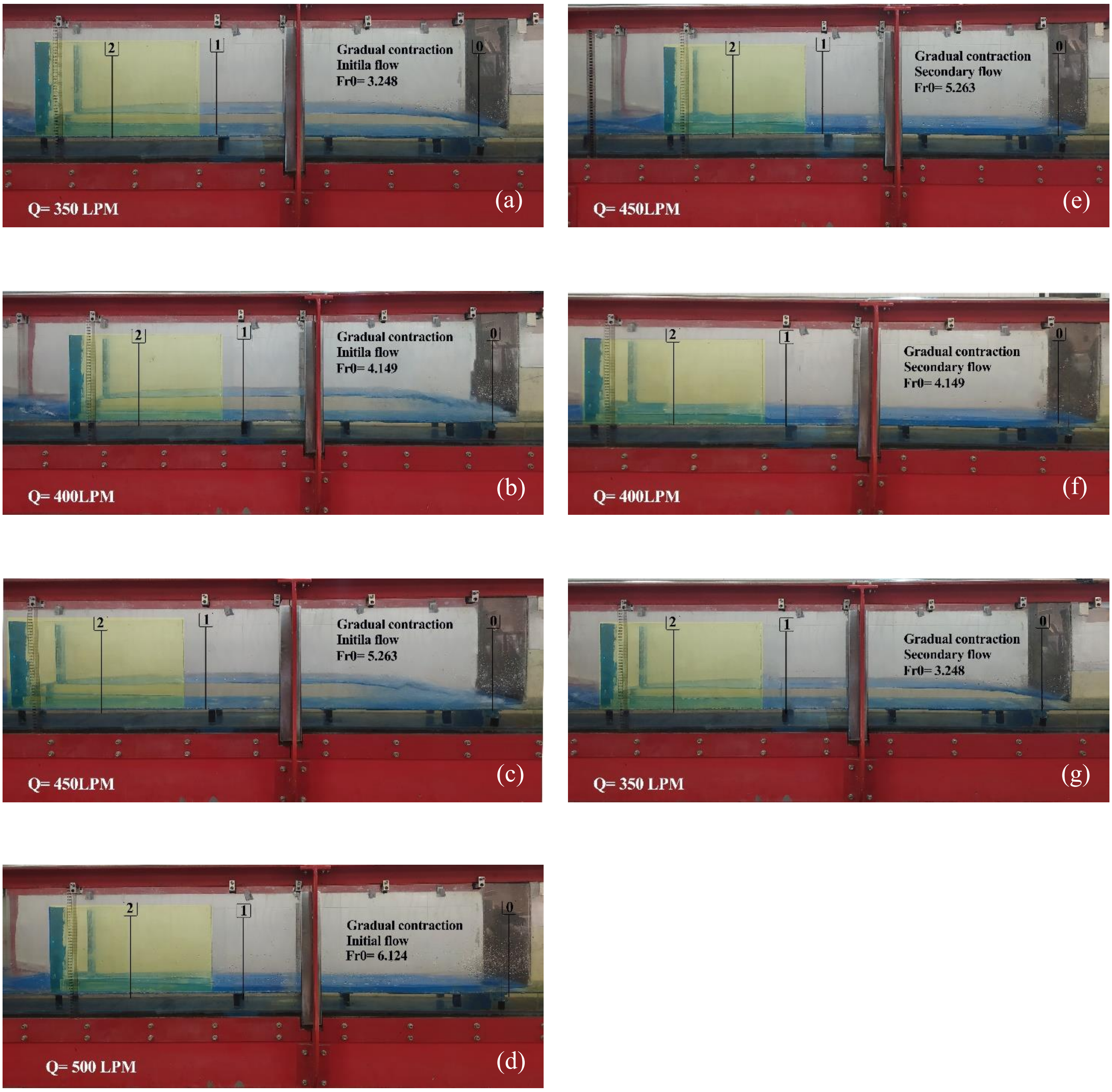

Figure 5. CS4 Experimental test runs

3.3. Relative Residual Energy

Investigating the effect of hysteresis on the amount of relative residual energy against the elements of sudden and gradual constriction, it was concluded that the emergence of hysteretic behavior in a number of discharges under the same input conditions causes a sharp increase in relative residual energy. This was observed in all models of the present study except the model of sudden contracting with a size of 15 cm. Figures 5 show the variation of relative residual energy versus the *vena contracta* Froude number and the effect of the hysteresis phenomenon on it in sudden constrictions of sizes 5 and 10 and gradual constriction. Figure (5a) shows the diagrams of the relative residual energy in section 1 and Figure (5b) shows the diagrams of the relative residual energy in section 2.

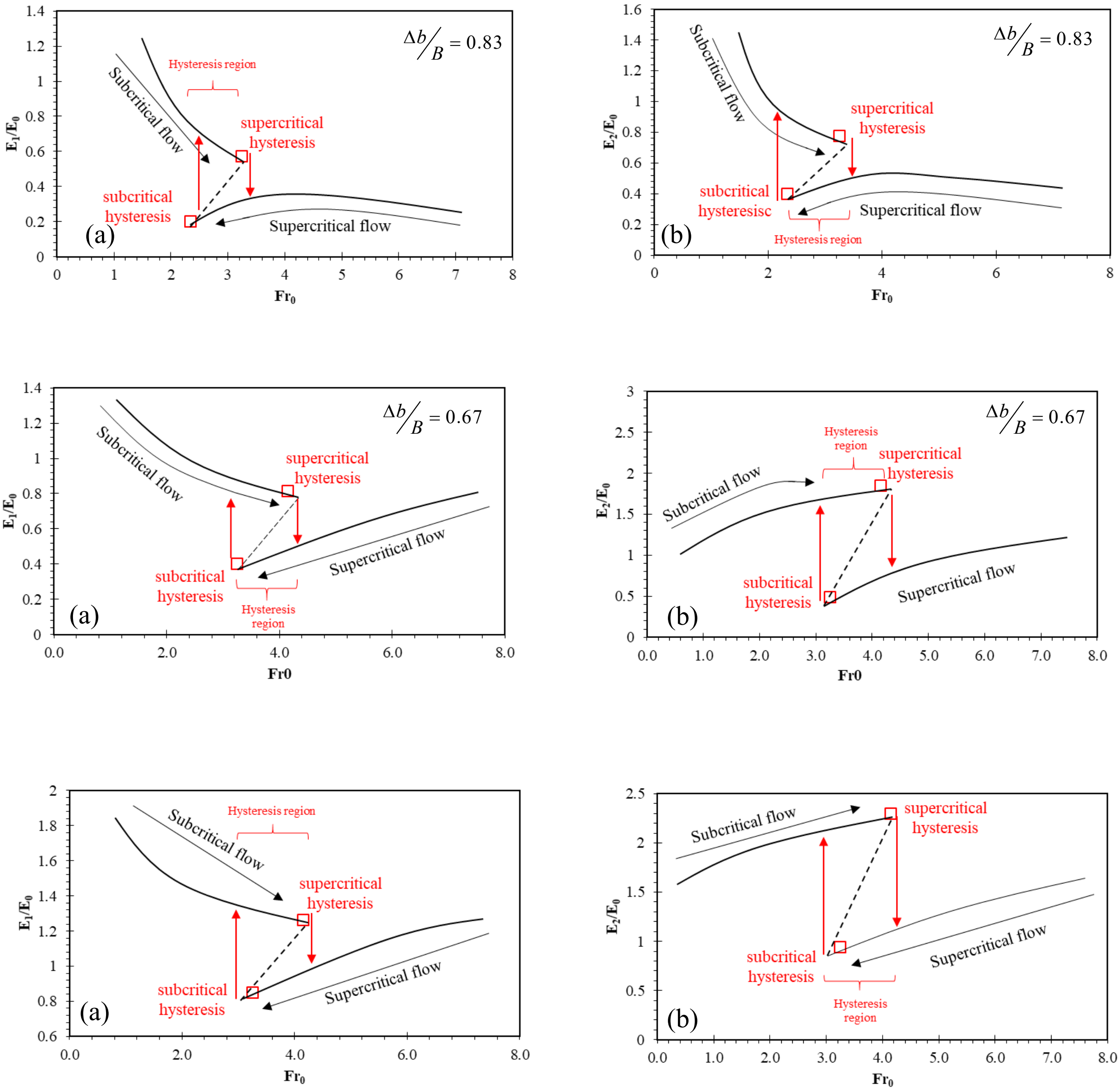

Figure 5. Influence of hysteresis phenomenon on relative residual energy in model CS1, CS2 and CS4: (a) Section 1 (b) Section 2

Examining the above figures, it is clear that the hysteretic behavior is clearly visible in these three models. In this case, with increasing flow rate in all three models, in lower flow rates due to the formation of hydraulic jump, the relative residual energy decreases and then with increasing flow rate and subsequent increase in flow velocity, the hydraulic jump moves downstream. In fact, the flow reaches a point shown on the figures as subcritical hysteresis. In this case, the control section is in supercritical mode and the relative residual energy is reduced. Then, by gradually reducing the flow rate to the initial value in the discharges that were in the upstream flow, the flow regime was subcritical, according to its previous state, it is placed in the supercritical regime.

In the present study, hysteretic behavior shows its effect in sudden contraction of 5 cm in the range of Froude number $2.33 \le Fr_0 \le 3.248$ and in sudden contraction of 10 cm and gradual contraction in the range of Froude number $3.248 \le Fr_0 \le 4.149$. In other words, the Froude number in range $Fr_0 > 4.149$ of the hysteresis phenomenon is out of control section. With the formation of hysteresis in the control sections of the present study, the relative residual energy increased sharply so that this value increased by 65.1% and 48.25% in sections 1 and 2, respectively, in the contracting of 5 cm, 50.79 and 73.51% in the contracting of 10 cm and 32.54 and 46.08% in gradual contracting. The effect of hysteresis on the contracting of 10 cm is more than other models. The reason for this is that with the collision of the flow with the constricted elements of 10 cm, the mixing water and bubbles interference in the increasing flow rate is high and with the formation of the hysteresis phenomenon following the reduction of the flow, the hydraulic jump disappears and the flow depth decreases sharply. The results show that gradual contracting has the least effect on the phenomenon of hysteresis and the greatest effect of hysteretic behavior on the hydraulic parameters of the flow in the sudden contracting of 10 cm. In other words, with the increase of sudden contracting, the hysteresis range becomes wider and causes a noticeable change in the values of the parameters. Table 3 shows the effect of hysteretic behavior on the relative residual energy parameter and the percentages of increase of these parameters.

Table 4. Percentage increase in the values of relative residual energy affected by hysterical behavior

Parameter / Model	E_1/E_0	E_2/E_0
CS 1	65.10%	48.25%
CS 2	50.79%	73.51%
CS 3	----	----
CS 4	32.54%	46.80%

By examining the sudden contracting of 15 cm, it was found that due to the reduction of the volume of the flow passage space, the hydraulic jump created in this case is of the submerged type and for this reason, the hysteresis phenomenon did not appear in all increased and decreasing flow rates. The relative residual energy in sections 1 and 2 decreases as the *vena contracta* Froude numbers increases. Figure 6 shows the relative residual energy variation in the 15 cm constriction in both sections. Therefore, with a huge increase in the amount of relative residual energy and the formation of a supercritical regime throughout the canal, in addition to the destruction and erosion of downstream structures and the canal bed, the aquatic life in these structures is lost and significant damage.

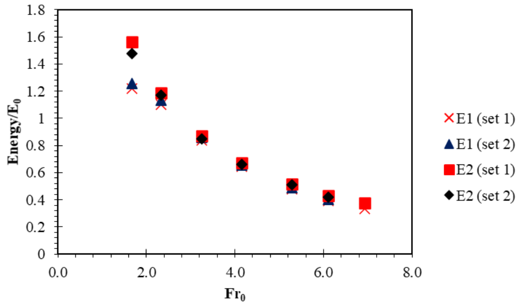

Figure 6. Variation of relative residual energy versus *vena contracta* Froude number in model CS3

In classical open canal hydraulics, the specific energy is a function of flow depth and velocity, with a minimum occurring at the critical flow condition. Under steady flow conditions without energy loss, this principle holds true. However, in the presence of hysteretic behavior as observed in this study the relationship between specific energy and flow depth does not follow a unique path.

The experiments demonstrate that for the same total discharge and geometric boundary conditions, the system can exhibit multiple steady states, specifically subcritical or supercritical regimes, depending on the flow history (i.e., whether flow is increasing or decreasing). This phenomenon leads to non-uniqueness in specific energy values, challenging the assumption of a single-valued specific energy-depth relation.

The observed increases in relative residual energy during hysteresis loops are indicative of this deviation from classical theory. While energy conservation still applies globally, local energy transitions particularly in the vicinity of hydraulic jumps or during regime shifts introduce energy losses and redistribution not accounted for by the traditional specific energy curve. Therefore, the hysteresis phenomenon does not violate the fundamental energy conservation principle but reveals limitations in the application of the specific energy concept in systems experiencing path-dependent (history-based) transitions.

3.4. Flow Regime (Froude number)

Figures 7a and b show the variations of the Froude numbers in sections 1 and 2, respectively, against the *vena contracta* Froude number. By increasing the flow rate and then decreasing it, two *vena contracta* Froude values occur under the same laboratory conditions. In sections 1 and 2, the subcritical flow becomes supercritical. In other words, with the CS3 model, the range over which hysteretic behavior is observed is $4.15 \le Fr_0 \le 5.26$. During the return to the initial flows (decreasing flowrate), sections 1 and 2 are in the subcritical regime.

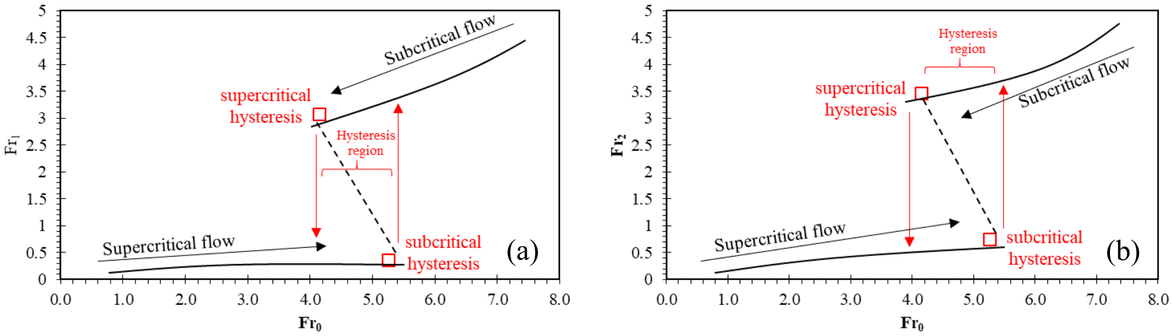

Figure 7. Variation of Froude number Vs. *vena contracta* Froude number in model CS4. (a) Section 1 (b) Section 2

Table 5 examines the effect of hysteretic behavior on hydraulic parameters and shows the percentages of decrease or increase in the amount of these parameters. In this table, it can be seen that the effect of hysteresis phenomenon on these parameters is very high and if this phenomenon is not studied in the design of hydraulic structures, it can cause irreparable damage. In the table below, a positive sign indicates an increase, and a negative sign indicates a decrease in the desired parameter values by forming a hysterical behavior.

Table 5. Percentage increase or decrease in the values of hydraulic parameters affected by hysterical behavior

Model \ Parameter	y_1/y_0	y_2/y_0	y_1/y_2	Fr_1	Fr_2
CS 1	-49.81%	-45.11%	-50.69%	+66%	+67.21%
CS 2	-72.50%	-56.76%	-69.76%	+80.97%	+63.66%
CS 3	----	----	----	----	----
CS 4	-69.66%	-61.23%	-48.21%	+88.50%	+87.29%

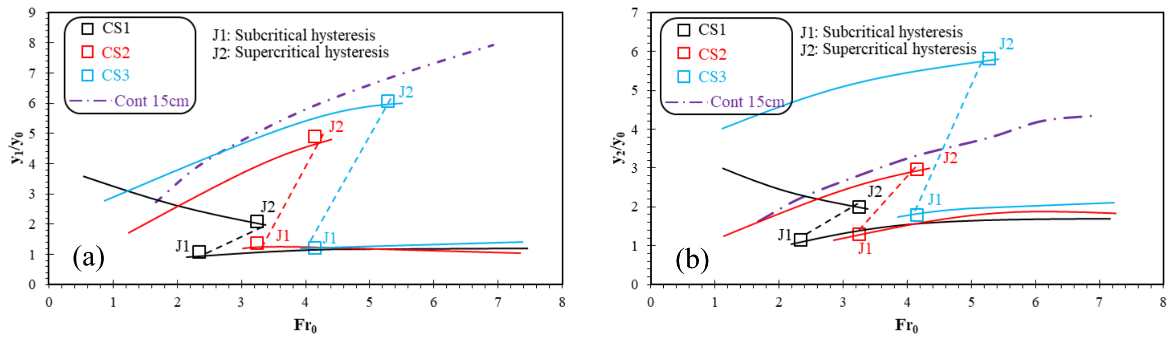

Figure 8. Comparison of relative depths: (a) Section 1 (b) Section 2

Figure 8 shows a comparison of the models in the present study with a sudden contraction of 15 cm. It is found that with a higher rate of sudden contraction, the wider the hysteresis region. Also, for gradual contraction, the hysteresis region is wider than for sudden contraction. Consequently, the hysteresis range is larger for the CS3 model than the CS2 model and more in CS2 than CS1.

4. CONCLUSIONS

Hydraulic jumps are a phenomenon that occurs in hydraulic structures with an obstacle in the flow path. There are no closed form equations to capture this phenomenon because of the nonlinearity. The hysteretic behavior of the flow causes different states in the flow, even though laboratory conditions may be similar. The issue of hysteresis in hydraulic structures should be considered by designers. In the present study, multiple canal contractions were utilized. Three models of contraction are sudden with dimensions of 5, 10 and 15 cm and another model were a gradual contraction with the size of the contraction 15 cm. Initially, the flow was increased from 250 to 600 liters per minute in 50 liter/minute increments. The second flow situation occurred when the flow decreased from 600 to 250 liters per minute, also in increments of 50. Two surface profiles are observed in an identical laboratory system, which are: 1) Profile 1: where sections 1 and 2 are subcritical and mode 2) Profile 2: where sections 1 and 2 are supercritical.

- Examining the results, it was observed that the hysteretic behavior during the supercritical regime was observed in all models except one. The sole model that did not display hysteresis experienced a hydraulic jump.
- In the CS1 model (a sudden contracting of 5 cm), hysteresis occurs in the range $2.3 \le Fr_0 \le 3.24$. When the flow rate increases to more than 350 liters per minute, the flow is supercritical. When the flow decreases to less than 300 liters per minute, the flow returns to subcritical.
- In the CS2 model (a sudden contraction of 10 cm), hysteresis occurs in the range $3.248 \le Fr_0 \le 4.149$. When the flow rate increases to more than 400 liters per minute, the flow is supercritical. When the flow decreases to less than 350 liters per minute, the flow returns to subcritical.
- In the CS4 model (a gradual contraction of 15 cm), hysteresis occurs in the range $3.248 \le Fr_0 \le 4.149$. When the flow rate increases to more than 400 liters per minute, the flow is supercritical. When the flow decreases to less than 350 liters per minute, the flow returns to subcritical. Use of sudden 15 cm contraction caused the formation of a submerged hydraulic jump for all discharges used in the present study and the hydraulic jump was unable to pass through the contracting area and therefore no hysteretic behavior was observed.
- As the rate of sudden contraction increases, the hysteresis region widens. Also, for gradual contractions, the hysteresis region is wider than for a sudden contraction, so that the hysteresis range is larger for CS4 model than for CS2 model and greater for CS2 than CS1.
- The hysteresis phenomenon increases the amount of relative residual energy in all models of the present study. The formation of hysteresis phenomenon increases the relative residual energy by an average of 49.47% in section 1 and by 56.18% in section 2.

REFERENCES

[1] Abecasis, F.M., and Quintela, AC. 1964. Hysteresis in steady free-surface flow. Water Power. 16, 147–151.

[2] Baines, P.G., and Davies, P.A. 1980. Laboratory studies of topographic effects in rotating and /or stratified fluids. In: WMO Orographic Effects in Planetary Flows. 1, 233–299.

[3] Austria, P.M. 1987. Catastrophe model for the forced hydraulic jump. Journal of Hydraulic research. 25, 269–280.

[4] Lawrence, G.A. 1987. Steady flow over an obstacle. Journal of Hydraulic Engineering. 113, 981-991.

[5] Baines, P.G., and Whitehead, J.A. 2003. On multiple states in single-layer flows. Physics of Fluids. 15, 298-307.

[6] Defina, A., and Susin, F.M. 2006. Multiple states in open channel flow. Vorticity and Turbulence Effects in Fluid Structures Interactions. 105-130.

[7] Akers, B., and Bokhove, O. 2008. Hydraulic flow through a channel contraction: Multiple steady states. Physics of Fluids. 20, 1-15.

[8] Defina, A., Viero, D.P. 2010. Open channel flow through a linear contraction. Physics of Fluids. 22: 1-12.

[9] Sadeghfam, S., Khatibi, R., Hassanzadeh, Y., Daneshfaraz, R., Ghorbani, M.A. 2017. Forced hydraulic jumps described by classic hydraulic equations reproducing cusp catastrophe features. Arabian Journal for Science and Engineering. 42, 4169-4179.

[10] Daneshfaraz, R., Aminvash, E., Ebadzadeh, P. 2023a. Experimental study of the effect of different sill geometry on hysteretic behavior of supercritical regime. Irrigation Sciences and Engineering. 46, 1-15 [In Persian].

[11] Viero, D.P., and Defina, A. 2018. Multiple states in the flow through a sluice gate. Journal of Hydraulic Research. 57, 39-50.

[12] Daneshfaraz, R., Aminvash, E., Sadeghfam, S. 2023b. Laboratory and theoretical study of hysteretic effects on hydraulic characteristics of flow at the site of smooth to rough bed conversion. Iranian Journal of Science and Technology, Transactions of Civil Engineering. 47, 3975-3987.

[13] Aminvash, E., Daneshfaraz, R., Sadeghfam, S., Mousavi, S. B. 2024. Laboratory investigation of the effect of hysteresis phenomenon of supercritical flow on the rough bed on the relative residual energy parameter. Journal of Hydraulic Structures. 10, 82-92.

[14] Daneshfaraz, R., Aminvash, E., Najibi, A. 2022. Experimental study of hysteretic behavior of supercritical regime on hydraulic parameters of flow against gabion contraction. Iranian Journal of Soil and Water Research. 53, 33-44 [In Persian].

[15] Aminvash, E., Daneshfaraz, R., Sume, V., Sadeghfam, S., Abraham, J. 2024. On the Multiple Steady Flow States in Spindle Shaped Geometry of Bridge Foundations. Journal of Applied Fluid Mechanics. 18(1), 1-15.

[16]. Daneshfaraz, R., Aminvash, E., Esmaeli, R., Sadeghfam, S., Abraham, J. 2020. Experimental and numerical investigation for energy dissipation of supercritical flow in sudden contractions. Journal of groundwater science and engineering. 8, 396-406.

[17] Daneshfaraz, R., Aminvash, E., Ghaderi, A., Kuriqi, A., Abraham, J. 2021. Three-dimensional investigation of hydraulic properties of vertical drop in the presence of step and grid dissipators. Symmetry. 13, 895.

[18] Abbaszadeh, H., Daneshfaraz, R., Sume, V., Abraham, J. 2024. Experimental investigation and application of soft computing models for predicting flow energy loss in arc-shaped constrictions. AQUA—Water Infrastructure, Ecosystems and Society. 73, 637-661.